Predictive all-atom simulations of disordered proteins and biomolecular condensates through osmometry-guided force-field optimization

Miloš T. Ivanović,[*,†] Valentin von Roten,[†] Benjamin Schuler,[*,‡] and Robert B. Best[*,¶]

†*Department of Biochemistry, University of Zurich, Winterthurerstrasse 190, 8057 Zurich, Switzerland*

‡*Department of Biochemistry and Department of Physics, University of Zurich, Winterthurerstrasse 190, 8057 Zurich, Switzerland*

¶*Laboratory of Chemical Physics, National Institute of Diabetes and Digestive and Kidney Diseases, National Institutes of Health, Bethesda, MD, 20892-0520, U.S.A.*

E-mail: m.ivanovic@bioc.uzh.ch; schuler@bioc.uzh.ch; robert.best2@nih.gov

Abstract

All-atom simulations with explicit solvent provide the most detailed and accurate description of dynamics and mechanisms in intrinsically disordered proteins and their condensates. However, interactions involving charged residues and ions remain a persistent source of systematic error. Here we introduce an osmometry-guided optimization strategy that directly targets residue–residue, residue–ion and ion–ion interactions. Osmotic pressure provides key experimental information on molecular interactions and can be calculated directly and rapidly from simulations, enabling efficient iterative force-field optimization. The resulting parameters improve agreement of all-atom simulations with a range of experimental data: single-molecule FRET measurements for 16 monomeric intrinsically disordered regions; NMR relaxation data for a complex between an IDP and a folded protein domain; and mean FRET efficiencies and chain reconfiguration times of IDPs in biomolecular condensates of highly charged proteins. For such condensates, simulations with an osmometry-calibrated force field provide the missing link for predicting condensate dynamics across length and time scales. The presented optimization strategy is broadly extensible to other interaction classes, including those governing protein–DNA and protein–RNA assemblies.

Intrinsically disordered proteins (IDPs) and intrinsically disordered regions (IDRs) are central to signaling, transcription, molecular recognition and the organization of cellular assemblies.[1] Rather than adopting one stable structure, they populate heterogeneous conformational ensembles whose populations and dynamics respond to sequence, binding partners, post-translational modification and solution conditions. These properties allow an IDR to recognize several partners, couple binding to regulation and remain dynamic within high-affinity complexes.[1–3] IDPs and IDRs are also major constituents of biomolecular condensates, concentrated and dynamic assemblies generated by multivalent interactions among proteins and often DNA or RNA,[4] which have been implicated in signaling, ribosome biogenesis, genome organization, transcription and stress responses.[1,5,6] The broad structural ensemble populated by IDRs also makes them difficult to model, since agreement with a sin-

gle average observable does not ensure that the underlying conformational ensemble, contacts or timescales are correct.[7] We thus require molecular models with the power to accurately predict IDP conformational heterogeneity and dynamics. In condensates, this challenge is amplified because these properties depend not only on intramolecular interactions but also on many transient intermolecular contacts in a concentrated, often multicomponent environment.[8]

Coarse-grained models have long been the workhorse of condensate simulations because they can reach the system sizes and statistical sampling needed to calculate phase diagrams, compare sequences and investigate material-property trends.[9–11] However, time scales from coarse-grained dynamics are generally much too fast and can only approximately be rescaled for comparison with experiment, owing to the many degrees of freedom omitted.[8,11] All-atom explicit-solvent force fields are able to play a complementary role to coarse-grained models: once optimized, the same model can be applied without system-specific parameter adjustment to monomeric IDPs, protein complexes and condensates, including systems containing both disordered and folded proteins, and its dynamics can be directly compared with experiment on an absolute time axis.[11–14]

Recent advances in accelerator hardware and molecular-dynamics software are making all-atom condensate simulations increasingly feasible. For example, systems containing several million atoms can now be followed for several microseconds,[13] but it is still critical to have an accurate energy function (force field): because of their disorder, IDRs can substantially shift their configurational ensembles in response to force field errors, in contrast to the more robust situation for folded proteins. Over the past decade, protein force fields have improved markedly through refinements of backbone and side-chain torsions,[15–17] protein–water interactions[18–22] and, in some models, electronic polarization.[17,23] These developments have enabled equilibrium folding calculations[24] and realistic simulations of both folded and disordered proteins.[21,25,26] Interactions between charged groups nevertheless remain a persistent weakness of widely used pairwise-additive models.[27,28] Association measurements on

side-chain analogues and NMR estimates of salt-bridge populations indicate that oppositely charged groups are too strongly associated in simulation.[27,29] In a sequence-diverse set of 16 IDRs, deviations between simulated and experimental mean Förster resonance energy transfer (FRET) efficiencies were most strongly correlated with the fraction of charged residues and the number of possible salt bridges; reweighting indicated the largest corrections for arginine-containing salt bridges.[30]

Including explicit electronic polarizability would provide a more physically realistic form for Coulomb interactions in force fields, but polarizable force fields remain four- to ten-fold more expensive and are not yet routine for the multi-million-atom, multi-microsecond calculations considered here.[31] Two practical corrections to interactions between charged groups have been successfully used within pairwise-additive models. Electronic-continuum-correction approaches scale ionic or charged-group partial charges to represent electronic screening implicitly.[32–35] Pair-specific Lennard-Jones terms instead rebalance selected short-range interactions without changing the net charge of a molecule.[36] However, identifying accurate corrections requires stringent benchmarks, ideally based on experimental data.

Osmotic pressure measurements are a promising source of information on intermolecular and interatomic interactions in solution and can be calculated directly and quickly for the same solution composition in simulation.[36–38]

Here we develop an osmometry-guided workflow for optimizing charge interactions in all-atom force fields (Fig. 1). We augment the limited available osmotic pressure data for monovalent salts and some amino acids with new, tailored experiments, particularly targeting interactions between charged residues. We derive two force field parameter sets that each reproduce the experimental observations: one based primarily on charge scaling and another that preserves integral charges while modifying Lennard-Jones interactions.

We assess the optimized parameters against a large set of experimental data: single-molecule FRET measurements for 16 sequence-diverse IDRs, NMR relaxation data for a highly charged complex between an IDP and a protein containing a folded domain, and

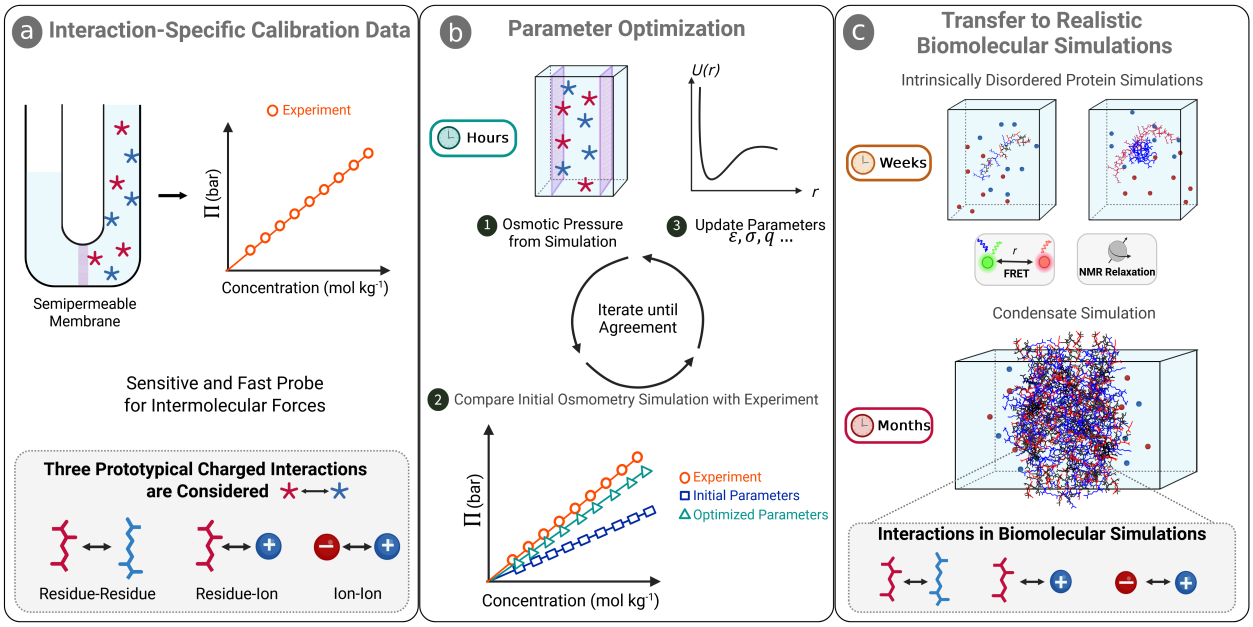

Figure 1: Osmometry-guided optimization and validation of charge interactions in all-atom force fields. a, Osmotic pressure, Π, is measured for defined solutions that isolate residue–residue, residue–ion and ion–ion interactions. A semipermeable membrane confines the solutes to one side while water passes freely allowing the osmotic pressure to be determined from the difference in height of the liquid in the columns on either side. Blue and red denote positively and negatively charged species, respectively. Star-shaped symbols represent generic charged solutes, water is light blue and the membrane is purple. **b,** Simulated and experimental concentration-dependent osmotic pressures identify interactions that are too attractive or too weak. In simulations, osmotic pressure can be calculated from the total force exerted on virtual semipermeable walls that mimic an osmotic membrane. Non-bonded parameters controlling Coulomb and Lennard-Jones interactions, including q, σ and ϵ, are varied iteratively until the benchmark is reproduced. **c,** Final parameters are transferred without further adjustment to explicit-solvent simulations of IDPs, protein complexes and condensates and validated against FRET, NMR and nsFCS. The calibration systems converge within hours, whereas the production simulations require weeks to months. Molecular sizes are schematic and not drawn to scale.

single-molecule FRET and nanosecond fluorescence correlation spectroscopy (nsFCS) measurements for four multicomponent condensates formed by charged disordered proteins. Residue-specific Lennard-Jones optimization yields a consistent overall improvement against this validation data set. Together, these results demonstrate that force field parameters optimized using osmotic pressures of simple amino acid and ion solutions transfer without further adjustment to proteins and multicomponent condensates. Because the solutes can be selected to target the interaction class of interest, the approach provides a simple and broadly applicable experimentally based strategy for optimizing problematic force field interactions.

Results

Osmotic pressure as a sensitive measure of molecular interactions

To achieve high efficiency, the workflow separates force-field optimization into calibration and validation stages that differ in molecular and computational complexity by several orders of magnitude (Fig. 1). Osmotic pressures are first measured for solutions chosen to isolate classes of interactions between charged moieties that recur in biomolecular simulations (Fig. 1a). The present set comprises oppositely charged amino acid pairs, charged amino acids with monovalent counterions, and NaCl or KCl. These mixtures retain the relevant chemical groups while avoiding the conformational heterogeneity of a protein and the coupled interaction network of a condensate. In particular, the side-chains already occur in the context of an amino acid, eliminating the need to assume that parameters can be "transferred" from small molecule analogs.[39] The experimental compositions are reproduced in simulation using semipermeable walls to mimic an osmotic membrane. The walls confine the solutes to a central region while water exchanges freely, and the osmotic pressure is calculated from the mean restoring force acting on the confined solutes.[36] Experiment and simulation are thus compared through the concentration dependence of the same thermodynamic observable. Candidate electrostatic or Lennard-Jones parameters are varied until the simulated osmotic pressures reproduce the measurements across interaction pairs and concentrations (Fig. 1b), rather than at a single state point. Finally, the optimized parameters are applied without further modification to realistic biomolecular systems and validated against multiple experimental observables (Fig. 1c).

A benchmark dataset resolves the relative strengths of charge interactions

For a solution of non-interacting solute species, the ideal osmotic pressure is

$$\Pi_{\text{ideal}} = c_{\text{tot}} RT,$$

where $c_{\mathrm{tot}} = \sum_i c_i$ is the total molar concentration of all solute particles, with each dissociated ionic species counted separately, R is the molar gas constant and T is the absolute temperature Attractions between solute molecules tend to lower Π relative to Π_{ideal}, whereas repulsive interactions have the opposite effect. The osmotic coefficient, $\phi = \Pi/\Pi_{\mathrm{ideal}}$, thus reports the net balance of solute–solute and solute–solvent interactions. Solution compositions in this work are reported as molalities, whereas c in the ideal-gas relation denotes molar concentration. The conversion of measured osmolality to the pressure scale is described in Methods.

We measured concentration-dependent osmotic pressures for equimolar Lys–Glu, Lys–Asp, Arg–Glu and Arg–Asp mixtures, and for Asp–Na^+ and Asp–K^+ solutions. Literature measurements for the remaining residue–ion and ion–ion pairs completed the benchmark.[40–42] Together, the data cover the basic and acidic side chains and the monovalent ions used throughout the subsequent protein simulations. Measurements over a concentration range are important because a force field may agree near the dilute limit yet deviate as weak pair interactions accumulate.

The measurements reveal substantial chemical specificity (Fig. 2). KCl and KGlu remain close to ideal over much of the investigated range, whereas most other pairs have osmotic coefficients below one, consistent with net attraction. At high concentration, NaCl instead reaches $\phi > 1$. The strength inferred for amino acid association follows Arg–Asp > Arg–Glu > Lys–Asp > Lys–Glu (Fig. S1a). For amino acid–ion pairs, the corresponding order is Arg–Cl^- > Asp–K^+ > Lys–Cl^- > Asp–Na^+ > Glu–Na^+ > Glu–K^+ (Fig. S1b). The pronounced Arg vs. Lys difference is qualitatively consistent with previous studies showing substantially stronger Arg-dependent interactions in IDPs and condensates.[13,43,44] Controlled substitutions in charge-patterned IDPs further show the same qualitative residue specificity in single-chain behavior: replacing Lys by Arg has a large effect on salt-dependent chain expansion, whereas replacing Glu by Asp has a much smaller effect.[45] The pair-resolved dataset consequently tests whether a force field reproduces both the relative and overall

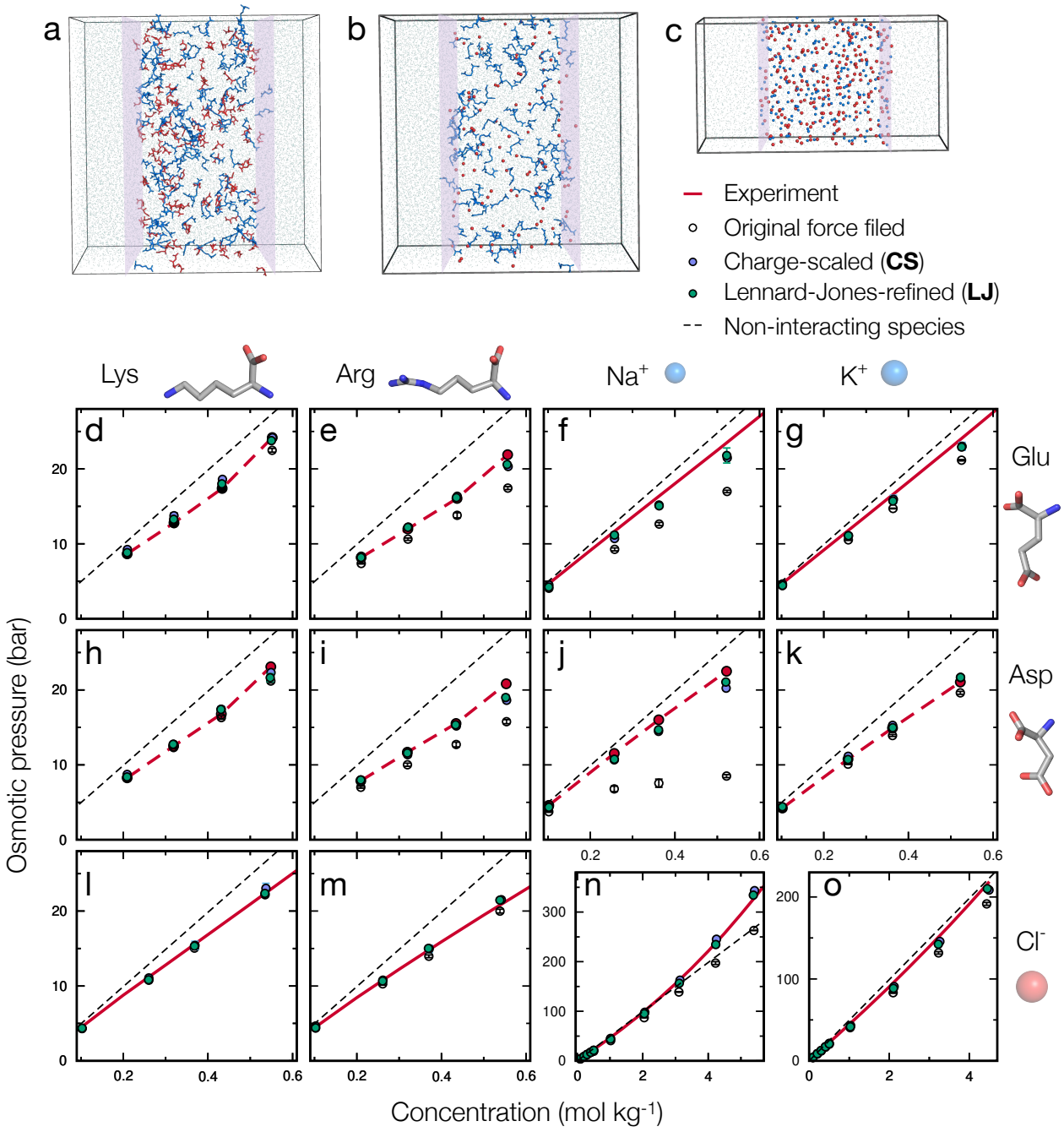

Figure 2: Osmometry benchmark and optimization of charge interactions. a–c, Representative simulation systems isolating residue–residue, residue–ion and ion–ion interactions. Positive species are blue, negative species red, water oxygens light blue and virtual semipermeable walls purple; hydrogen atoms are omitted. **d–o,** Experimental osmotic pressures (red lines) are compared with corresponding values calculated using three force fields: the original Amber ff99SBws (black circles), charge-scaled Amber ff99SBws-CS (purple circles), and Lennard-Jones-refined Amber ff99SBws-LJ (green circles). Vapor-pressure-osmometry measurements for Lys–Glu, Lys–Asp, Arg–Glu, Arg–Asp, Asp–Na^+ and Asp–K^+ were obtained in this work; the remaining experimental values were taken from the literature.[40–42] Simulated osmotic pressures below the corresponding experimental values indicate excessive net attraction. The black dashed line indicates the dependence expected for non-interacting species. Experimental and simulation uncertainties are defined in Methods. Most error bars are smaller than the plotting symbols.

strengths of charge interactions.

We calculated the corresponding osmotic-pressure curves based on simulations with Amber ff99SBws and TIP4P/2005 water, using the Luo–Roux monovalent-ion parameters as the starting point.[18,36,46] Because standard Amber protein force fields do not provide a parameter set for isolated amino acids with both termini charged, we derived a shared zwitterionic backbone while retaining the protein-force-field side-chain charges (Methods). Simulations of zwitterionic alanine and glycine agreed with our measurements and literature data[47,48] (Fig. S2) without adjustment, validating the terminal-group model.

The original force field reproduced several interaction pairs reasonably but underestimated Π for important combinations, indicating excessive net attraction (Fig. 2). The largest deviations involved arginine and sodium together with anionic amino acids, and Asp–Na^+ showed the strongest discrepancy. This ordering is consistent with earlier measurements and calculations identifying overly favorable salt bridges in additive force fields.[27,29] It also mirrors the stronger correction inferred for arginine-containing salt bridges in our previous study.[30]

Two optimization routes reproduce the osmotic-pressure benchmark

We explored two force field optimization routes that alter the balance of solute–solute and solute–water interactions by prioritizing changes to different terms in the potential energy function. The first weakens Coulomb interactions by scaling the charges of charged residues and ions, followed by limited ion–water Lennard-Jones adjustments. The second preserves the integral net charges of residues and ions and more extensively modifies Lennard-Jones interactions.

Route 1: Charge scaling correction

Following the rationale of electronic-continuum-correction models,[32–35] we scaled the partial charges on the heavy atoms of charged side chains so that each side chain carried a net charge of $\pm q$ rather than $\pm 1e$. We scanned q using the four amino acid-pair datasets at four concentrations and evaluated the global discrepancy from experiment. A charge magnitude of $0.93e$ minimized the unreduced χ^2 (Fig. S3), reaching a value of 7.1 from an initial value of 45.6. Smaller charge magnitudes produced only modestly larger deviations, whereas the discrepancy increased rapidly above $0.93e$. We selected $0.93e$ as the least perturbative value within the optimum and applied the same magnitude to monovalent ions to preserve charge neutrality; this value is in a similar range to those obtained in several earlier studies.[22,34,49,50]

In addition to the residue–residue data, charge scaling also brought the residue–ion and ion–ion osmotic pressures closer to experiment, but interactions of Na^+ and K^+ with acidic residues remained too attractive, whereas Cl^- association with basic residues became slightly too weak. One electrostatic scaling factor changes every interaction involving a scaled site, including favorable and unfavorable Coulomb terms and its interaction with solvent. To further improve residue–ion and ion–ion parameters, we therefore adjusted the Lennard-Jones diameter σ between each inorganic ion and the water oxygen atom (OW), as related corrections have previously been required in charge-scaled models.[51,52] Relative to values from the standard combination rule, the selected scaling factors were 0.965 for $\sigma_{Na^+–OW}$, 0.98 for $\sigma_{K^+–OW}$ and 1.005 for $\sigma_{Cl^-–OW}$ (Fig. S4). The small $\sigma_{Cl^-–OW}$ change had little effect on the already reasonable Lys–Cl^- and Arg–Cl^- curves. Together with the cation–water adjustments, it allowed the NaCl and KCl osmotic pressures and coordination numbers to be described with the same parameter set. The set of parameters optimized via this route was denoted Amber ff99SBws-CS.

Route 2: Lennard-Jones optimization with integral charges

The second route retained the formal net charges of all residues and ions. We first changed σ for interactions between OW and the heavy atoms of charged amino acid side chains. A uniform 1% reduction across the four charged residues lowered the global χ^2 for the four residue-pair datasets from 45.6 to 6.0 (Fig. S5). Residue-specific optimization reduced it further, to 4.5. The selected $\sigma_{\text{residue–OW}}$ scaling factors were 0.99 for lysine, 0.985 for arginine, 0.99 for aspartate and 0.995 for glutamate. The largest change was thus assigned to arginine, in agreement with the correction inferred by reweighting the 16-IDR dataset.[30] Modifying $\sigma_{\text{residue–OW}}$ shifts the balance between hydration and direct residue association while leaving formal charge and long-range electrostatics unchanged.

These changes in $\sigma_{\text{residue–OW}}$ were sufficient for Lys–Cl^- and Arg–Cl^-, and improved, but did not fully correct, the interactions of acidic residues with Na^+ or K^+ (Fig. S6). We therefore modified the ion Lennard-Jones parameters. Across commonly used monovalent-ion parameter sets, σ and the well depth ϵ differ widely, but are strongly anticorrelated (Fig. S7a), likely because of the emphasis on parameterization using solvation free energy, which is strongly dependent on the ion radius.[53] Here, we preserved this relation while modifying the ion parameters. Defining the effective radius r_{eff} as the distance at which the ion–water Lennard-Jones energy reaches $\epsilon_{\text{rep}} = 0.5\,\text{kcal}\,\text{mol}^{-1}$, i.e. $r_{\text{eff}} = \sigma\left[2/(1+\sqrt{1+\epsilon_{\text{rep}}/\epsilon})\right]^{1/6}$, we varied σ and ϵ while changing r_{eff} by less than 2% (Fig. S7d).

Increasing σ_{K^+} weakened excessive Glu/Asp–K^+ association, whereas lowering ϵ_{K^+} partly opposed this change by shifting the competition between ion–water and residue–ion interactions. A 1.3-fold increase in σ_{K^+} together with a 0.02-fold scaling of ϵ_{K^+} best reproduced both acidic-residue datasets (Fig. S6c,d). For Na^+, the residue–water changes already reduced excessive Glu/Asp–Na^+ attraction. A further 1.3-fold increase in σ_{Na^+} improved the agreement, and setting $\sigma_{Na^+–OW}$ to its original force-field value gave the best result within this functional form (Fig. S6e,f). Asp–Na^+ remained somewhat too attractive, but further changes produced little improvement.

We finally tested ion–ion association, because changes made to improve residue–ion interactions can disrupt electrolyte behavior. The modified K^+ parameters alone overstabilized KCl at high concentration and increased the near-saturation coordination number from the experimental value of 0.6 ± 0.1 to 2.92 ± 0.03.[54] Pair-specific K^+–Cl^- parameters, with $\sigma_{K^+-Cl^-}$ and $\epsilon_{K^+-Cl^-}$ scaled by factors of 1.3 and 0.29, respectively, reproduced both the KCl osmotic-pressure curve and a coordination number of 0.50 ± 0.03, within error of the experimental value. The Na^+ changes had the opposite effect and made NaCl association too weak. Scaling $\epsilon_{Na^+-Cl^-}$ by 0.29 restored agreement with the osmotic-pressure data and increased the coordination number from 0.0006 to 0.22 ± 0.03, close to the experimental value of 0.3 ± 0.1.[54] These tests prevent a local improvement in amino acid–ion interactions from being obtained at the cost of an unphysical ion distribution. The complete set of parameters optimized via this route was denoted Amber ff99SBws-LJ.

Parameter testing in folded and disordered proteins

Altogether, charge scaling (CS) and Lennard-Jones (LJ) optimization both reproduce the calibration data set, but what are the consequences of these parameter changes for the transferability to more complex biomolecular systems? The parameters optimized in the small systems were transferred without further adjustment to more complex biomolecular simulations. The first test uses IDRs whose mean transfer efficiencies are measured by single-molecule FRET; the second introduces a folded binding partner and compares residue-resolved NMR relaxation; and the final test compares simulated and experimental mean transfer efficiencies and absolute chain reconfiguration times within multicomponent condensates using single-molecule FRET and nsFCS. Together, these comparisons assess the transferability of interaction parameters optimized using amino acid osmometry across monomeric disordered chains, protein complexes and condensates.

Improved consistency with FRET data for 16 disordered proteins

To determine whether agreement in the calibration systems transfers to proteins, we simulated 16 naturally occurring IDRs of identical length but diverse composition and charge patterning.[30,55] Their mean transfer efficiencies, which report on the average end-to-end distances, had previously been measured by single-molecule FRET, and each dye-labeled sequence was simulated explicitly with both optimized parameter sets. The original force field already captured the broad sequence dependence but yielded several chains that were too compact. The deviation from experiment correlated with the fraction of charged residues and even more strongly with the number of possible salt bridges.[30]

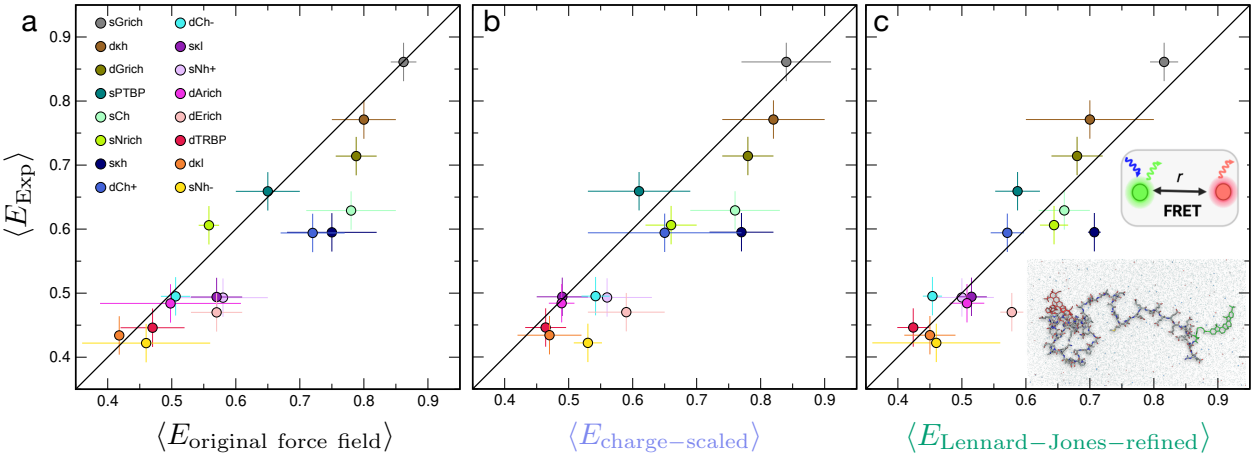

Figure 3: Transferability across sequence-diverse disordered proteins. Experimental mean FRET efficiencies for 16 IDRs of identical length are compared with values calculated from explicit-dye simulations using **a,** the original Amber ff99SBws force field, **b,** the charge-scaled parameters and **c,** the Lennard-Jones-modified parameters. Each color denotes one IDR (see legend). The concordance correlation coefficients are 0.84, 0.83 and 0.91, respectively. The inset shows an IDR with Cy3B (green) and CF660R (red), K^+ (blue), Cl^- (red) and water (transparent light blue); hydrogen atoms are omitted. Experimental and simulation uncertainties are defined in Methods and Refs. 30,55.

The constant chain length makes this set a sensitive test of sequence-dependent intrachain interactions. Differences in transfer efficiency therefore arise from amino acid composition and patterning rather than polymer length, while the explicit treatment of the fluorophores retains their steric and electrostatic contributions. The set includes chains with different fractions and arrangements of positive and negative residues, so an apparent improvement confined to one sequence cannot dominate the assessment. The results (Fig. 3) show that

the LJ variant improved the agreement with experiment (concordance correlation coefficient of 0.91 versus 0.84 for the original force field), with the largest reductions in error occurring among charge-rich sequences. The agreement of the scaled charge (CS) variant was similar to the original (concordance correlation coefficient of 0.83). We therefore selected the Lennard-Jones-refined parameter set, Amber ff99SBws-LJ, for additional testing on a folded–disordered complex and protein condensates.

Dynamics from NMR relaxation in a folded–disordered protein complex

We next examined the highly charged complex between the intrinsically disordered prothymosin α (ProTα) and the folded globular domain of histone H1,[3] whose structural and dynamic properties have been investigated in detail with NMR.[56] ProTα remains disordered in this high-affinity complex and rapidly exchanges among many configurations on the surface of its folded partner. The system combines electrostatic interactions, structural heterogeneity and a globular protein surface, features absent from both the osmometry solutions and the monomeric-IDR validation. It is also a stringent dynamic benchmark: over-stabilized intermolecular salt bridges can slow the exchange among configurations.[56]

NMR longitudinal and transverse relaxation rates (R_1 and R_2) and the steady-state heteronuclear NOE report on residue-specific backbone dynamics of ProTα. With the original force field, simulated R_2 rates for ProTα were substantially above the experimental values, especially in its highly charged C-terminal region (Fig. 4a). The excess R_2 corresponds to motion that is too slow on the nanosecond timescale and is consistent with long-lived intermolecular contacts. The Lennard-Jones-refined (LJ) force field improved both R_1 and R_2 across the ProTα sequence (Fig. 4a). Intermolecular contact lifetimes provide a molecular explanation: the mean lifetime of ProTα–H1 contacts decreased from 12.0 ± 1.0 ns with the original parameters to 6.3 ± 0.4 ns after optimization, and the long tail of contacts persisting for hundreds of nanoseconds was strongly suppressed (Fig. 4b). Overall, the parameters optimized using amino acid osmometry improve charge-driven interactions between a disordered

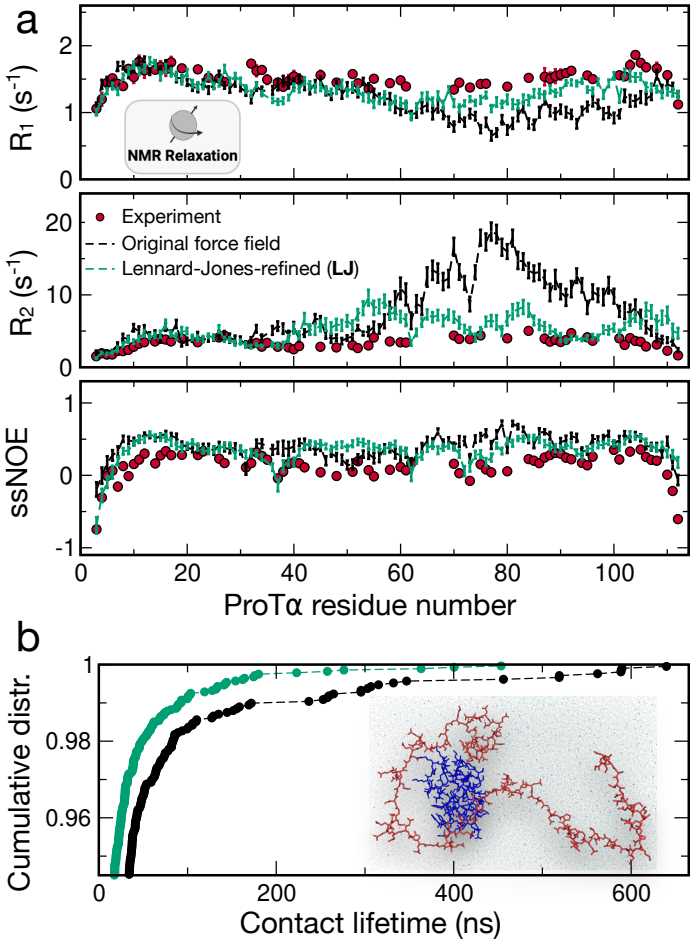

Figure 4: Dynamics of a complex between a folded domain and an IDP. a, Experimental residue-resolved R_1, R_2 and steady-state heteronuclear NOE values for ProTα bound to the globular domain of histone H1,[56] compared with values calculated using the original and Lennard-Jones-modified force fields. **b,** Cumulative distributions of intermolecular contact lifetimes. The optimized parameters suppress the tail of long-lived contacts present with the original force field. The inset shows ProTα (red), the H1 globular domain (blue), K^+ (blue spheres), Cl^- (red spheres) and water (transparent light blue); hydrogen atoms are omitted.

chain and a folded protein.

Optimized interactions match experimental chain dynamics within condensates

Multicomponent biomolecular condensates provide a demanding test because each protein samples a dense network of residue–residue and residue–ion interactions over a wide range of local environments. Small imperfections that are tolerable in a dilute solution can accumulate in the dense phase of a condensate, leading to kinetic trapping, an incorrect molecular density, or dynamics on the wrong absolute timescale. We previously used all-atom simulations to relate nanosecond chain reconfiguration to translational diffusion and bulk viscosity in complex coacervates composed of ProTα and different Lys- and Arg-rich polycations.[12,13] The simulations reproduced the qualitative slowdown from lysine-rich to arginine-rich condensates, but ProTα reconfiguration times in the arginine-rich systems were more than an order of magnitude longer than in experiment.[13] These condensates thus provide a stringent test of whether the parameters optimized using small-molecule solutions transfer to such large biomolecular assemblies.

We simulated ProTα condensates formed with either lysine-rich histone H1 or arginine-rich protamine at 8 mM and 128 mM KCl, yielding four systems of 2.6–4.0 million atoms. The two polycations provide a chemically informative comparison because arginine required a larger osmometry-derived correction than lysine. The two different salt concentrations are a further test of the balance of protein and ion interactions.

We first examined ProTα chain dimensions within the condensates using the mean FRET efficiency, $\langle E \rangle$, for direct comparison with experiment. Amber ff99SBws already reproduces the experimental transfer efficiencies for three of the four condensate conditions, with the remaining ProTα–protamine condensate at low salt showing a modest deviation. Amber ff99SBws-LJ preserves the agreement across all systems and improves the agreement for the ProTα–protamine condensate at low salt (Table S1).

The average ProTα reconfiguration times in the lysine-rich ProTα–H1 condensates were

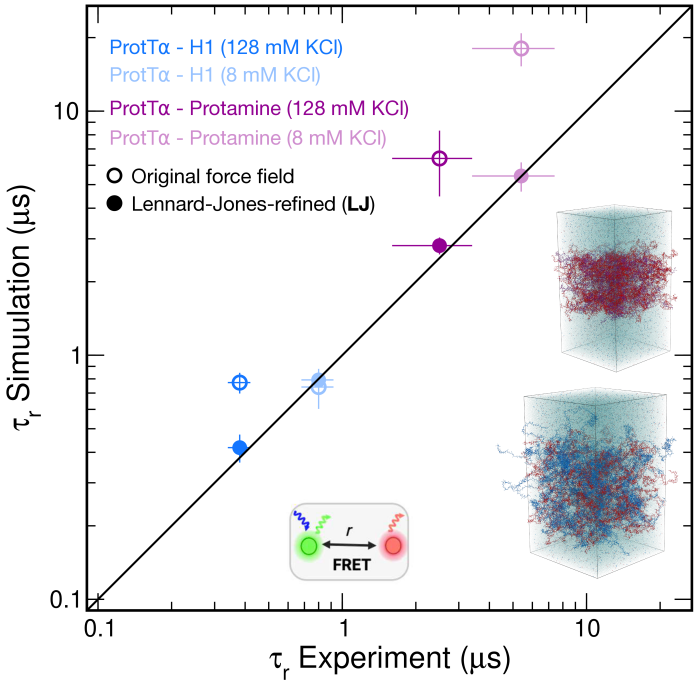

Figure 5: Absolute chain reconfiguration times in multicomponent condensates. ProTα chain reconfiguration times measured by nsFCS are compared with values calculated from all-atom simulations of condensates formed with lysine-rich H1 or arginine-rich protamine at 8 and 128 mM KCl. In the simulations, reconfiguration times were calculated by tracking the distance between ProTα residues 58 and 112, corresponding to the dye positions in the experiments; the exact procedure is described in Methods. For the low-salt ProTα–protamine condition, the simulation at 8 mM KCl is compared directly with the closest experimental measurement, obtained at 25 mM added KCl (approximately 33 mM total ionic strength), as done previously,[13] because nsFCS measurements at lower salt concentrations were not feasible. Numerical values and uncertainties are given in Table S1. Open and filled circles denote the original and Lennard-Jones-refined force fields, respectively; the diagonal denotes identity. Insets show representative ProTα conformations and simulation snapshots of the ProTα–H1 and ProTα–protamine condensates at 128 mM KCl. ProTα is red, H1 blue, protamine purple, K^+ blue, Cl^- red and water transparent light blue; hydrogen atoms are omitted.

already within the experimental range with the original force field. However, a subset of chains exhibited restricted motion, defined as a standard deviation of transfer efficiency below 0.05 over the course of the simulation, suggesting trapping within a rugged energy landscape. At 128 mM KCl, 23 of 96 ProTα chains exhibited restricted motion with Amber ff99SBws, which was reduced to 10 with Amber ff99SBws-LJ, while the overall reconfiguration time remained within the experimental range (Fig. 5). The Lennard-Jones modifications therefore reduce local kinetic trapping without affecting the agreement already obtained for the lysine-rich condensates.

Simulations with the original force field showed that, across the four simulated conden-

sates, the mean lifetime of intermolecular residue–residue contacts involving ProTα scales with the ProTα reconfiguration time.[13] We find a similar (even stronger) correlation between contact lifetimes and reconfiguration times with the new force field (Fig. S8). The correlation in both cases strongly suggests that transient residue–residue interactions are a key determinant of chain reconfiguration, through their contribution to the effective friction for chain motion.[13] Quantitatively reproducing reconfiguration times therefore requires an accurate balance of residue–residue interactions: by reducing overly strong salt bridges through osmometry-guided refinement, ff99SBws-LJ shortens contact lifetimes and brings chain reconfiguration into better agreement with experiment (Fig. 5). Because chain reconfiguration is in turn linked to mesoscopic condensate dynamics, this interaction balance is also critical for quantitatively describing condensate material properties.[13] The effect of the refinement is largest in the arginine-rich ProTα–protamine condensates. With f99SBws, ProTα reconfigured over an order of magnitude more slowly than in experiment, although the qualitative slowdown relative to the ProTα–H1 condensates was reproduced.[13] In simulations with ff99SBws-LJ, both protamine-containing systems are in much better agreement with the experimental values (Fig. 5). The largest improvement thus occurs in the condensates enriched in arginine, the residue requiring the largest correction in the osmometry-based optimization.

Discussion

We have shown that using a customized set of osmotic-pressure measurements, representing residue–residue, residue–ion and ion–ion interactions, we are able to optimize interactions among charged species in an all-atom force field. This procedure has a number of advantages: the solutes being probed are close to those in the final biomolecular force field, reducing the need for parameter transferability from model compounds to protein residues, yet the systems needed to compute osmotic pressure are small enough that it can be used in an iterative pa-

rameter refinement cycle. Only once the final optimized parameters are determined are larger scale biomolecular simulations required for testing. We found that the osmometry-guided optimization yielded improvements in both configurational and dynamic properties across all three biomolecular systems tested, with the most dramatic improvement being observed for the dynamics within arginine-rich condensates, consistent with the larger corrections to arginine required in the optimization. Notably, we were able to achieve similar accuracy with respect to osmotic pressure data with two different strategies, one (CS) prioritizing scaling of partial charges on residues with net charge, the other (LJ) keeping integral charges, but modifying Lennard-Jones parameters. The more accurate protein reconfiguration timescales in condensates that can be estimated using the optimized Amber ff99SBws-LJ force field also have important consequences because of the recently established polymer-physics relations connecting chain reconfiguration to translational diffusion and bulk viscosity:[13] corrections to molecular reconfiguration are therefore expected to result in improved estimatesof diffusion and material properties on larger scales.

The biological reach of charge-driven interactions extends well beyond protein salt bridges, as they are involved in mediating histone–DNA association, drive complexation of arginine-rich RNA-binding regions with RNA, and contribute to the assembly and selective composition of transcriptional, nucleolar and stress-associated condensates.[6,57,58] Protein–nucleic-acid interactions are therefore an important next application of the method, in particular the interaction of phosphate groups with basic protein side chains and ions. Conventional additive force fields can over-stabilize amine–phosphate interactions in peptide–nucleic-acid assemblies.[59] Osmotic-pressure measurements on amino acid–nucleotide and nucleotide–ion solutions could directly probe these interactions, followed by parameter optimization in the corresponding small simulations. Tests against protein–DNA and protein–RNA complexes would then establish whether the parameters transfer to heterogeneous biomolecular assemblies before they are used in simulations of nucleic-acid-containing condensates.

Finally, although we have focussed on a specific strategy for parameter optimization, the

osmometry measurements reported here also provide a resourcethat may be used by others for optimization of parameters in future force-field paradigms.

Methods

Osmometry measurements

L-Lysine monohydrate, L-arginine, L-glutamic acid, L-aspartic acid, L-aspartic acid potassium salt and L-aspartic acid sodium salt monohydrate were purchased from Sigma-Aldrich. Equimolar mixtures of oppositely charged amino acids (Lys–Glu, Lys–Asp, Arg–Glu and Arg–Asp) were prepared by combining L-lysine monohydrate or L-arginine with L-glutamic acid or L-aspartic acid. The amounts of the basic and acidic amino acids were determined by weighing each powder with a precision of 0.0003 g. The highest molality prepared for each amino acid pair was approximately $0.55\,\mathrm{mol\,kg^{-1}}$, with the exact value chosen to match the molality of the corresponding simulated system. Solutions of lower molality were prepared by dilution with ultrapure water. The water of crystallization in L-lysine monohydrate and L-aspartic acid sodium salt monohydrate was included when calculating the sample concentrations. Solutions containing Asp–Na^+ and Asp–K^+ were prepared by dissolving the corresponding purchased salts and subsequently diluting the resulting solutions. All osmometry measurements were performed using a VAPRO Vapor Pressure Osmometer 5600. Calibration was performed at the beginning of each measurement day using $100\,\mathrm{mOsm\,kg^{-1}}$, $290\,\mathrm{mOsm\,kg^{-1}}$ and $1000\,\mathrm{mOsm\,kg^{-1}}$ calibration standards. The standards were then remeasured until all three gave stable readings within $3\,\mathrm{mOsm\,kg^{-1}}$ of their nominal values.

Measured osmolality values were converted to osmotic pressure using $\Pi = c_{\mathrm{osm}} RT$, where c_{osm} is the measured osmolality expressed as the concentration of osmotically active particles, R is the gas constant and $T = 298.15\,\mathrm{K}$. For each of the six datasets shown in Fig. 2 (Lys–Glu, Lys–Asp, Arg–Glu, Arg–Asp, Asp–Na^+ and Asp–K^+), samples were prepared using at least two independently purchased batches, and every concentration point was

measured on at least two different days. At each concentration on each measurement day, three to six replicate measurements were performed and averaged to obtain a daily mean. The reported osmotic pressure for each concentration point was calculated as the mean of the daily means. Uncertainties for all reported osmotic-pressure values were estimated by combining in quadrature the manufacturer-specified instrumental uncertainty of 1% of the reported osmotic pressure and a calibration contribution corresponding to the $3\,\mathrm{mOsm\,kg^{-1}}$ calibration tolerance. At 298.15 K, the latter corresponds to 0.0744 bar, giving

$$\sigma_\Pi = \sqrt{(0.01\,\Pi)^2 + (0.0744\,\mathrm{bar})^2},$$

where Π is the reported osmotic pressure. For concentration points measured independently on at least three days, the standard deviations among the daily means were also calculated, which were similar to the corresponding values of σ_Π calculated above. The value of σ_Π calculated as shown above was therefore used as the uncertainty estimate for every reported osmotic-pressure value.

Derivation of force field parameters for amino acids with charged termini

Since the Amber force fields do not include standard parameters for single residues in which both termini are charged (i.e., zwitterions, in the case of a neutral side-chain), it was necessary to determine such parameters. We used the Amber Antechamber tool to automatically assign protein atom types and bonded parameters (angles, dihedrals) involving the terminal atoms, keeping the bonded parameters for the side-chain the same as in the protein force field. This left the atomic partial charges as the remaining critical parameter. For Amber force fields, partial charges are usually fitted to a molecular electrostatic potential via the RESP algorithm. However, we made several assumptions to reduce the degeneracy of the problem and to maximize similarity with the protein force field. First, we fixed the side-chain charges (i.e. those on the β position of the side-chain and beyond) to be identical

to those for each residue/amino acid in the standard protein force field, with the aim of improving transferability of the results. Second, we assumed that a common set of backbone charges should be used across all residues. This was motivated by the Cornell *et al.* force field (Amber 94)[60] and its many descendants using the same charges on backbone atoms for all internal residues, except for the residues with charged side-chains. We had subsequently found that using common charges for all residues (including charged residues) in fact resulted in improved prediction of α-helix propensity,[61] and this change was incorporated in the Amber 99SBws force field.[18] Therefore, the problem reduces to finding a set of charge differences (summing to zero) from the fixed charge set for internal residues. We determined these differences by (i) running a standard RESP fit[62] of charges to an electrostatic potential computed with the HF/6-31G basis set using Gaussian 16;[63] (ii) computing differences of the charges from those for interior residues for each of lysine, arginine, glutamate and aspartate; (iii) averaging the differences and subtracting their sum (0.0259) from the α carbon charge difference to give a net difference of zero; (iv) adding these differences to the standard force field charges. This scheme preserves the total charge of each residue. We applied the same backbone charges also to form the zwitterions of alanine and glycine. Scripts, notes and force field parameters for the residues with charged termini are available in the publication data repository.

All-atom osmometry simulations

Osmotic pressures were calculated from all-atom simulations using a virtual-semipermeable-wall approach based on the method introduced by Luo and Roux.[36] In their original implementation, Luo and Roux calculated osmotic pressures for concentrated NaCl and KCl aqueous solutions by confining the ions to a defined region of the simulation box with virtual walls, while allowing water molecules to move freely through the periodic system. The osmotic pressure was then obtained from the mean force exerted by the virtual walls on the confined solutes, divided by the wall area. Here, the virtual walls were implemented in

GROMACS[64] using flat-bottomed position restraints. Water molecules were not restrained and could diffuse freely throughout the simulation box. The solute particles used to calculate the osmotic pressure were free to diffuse in the x and y directions and within the defined slab along the z direction. When a restrained solute particle moved outside this slab, the flat-bottomed restraint applied a harmonic restoring force directed back toward the confined region. Thus, the restraints acted as idealized semipermeable walls that confined the solutes but not the water. The flat-bottomed restraints were applied with a layer geometry normal to the z direction. For atomic ions, the restraint was applied directly to the ion. For amino acid residues, the restraint was applied to the C_α atom of each residue. The same restraint parameters were assigned to all residues of a given type through the corresponding residue topology. The osmotic pressure was calculated from the force exerted by the virtual walls on the restrained solute particles, following Luo and Roux.[36] At each saved simulation frame, the force contribution from each restrained particle outside the flat-bottom region was calculated from the applied restraint. The force magnitudes from the two slab boundaries were averaged, and the osmotic pressure was calculated as

$$\Pi = \frac{\langle F_+ + F_- \rangle}{2A}, \tag{1}$$

where F_+ and F_- are the instantaneous force magnitudes exerted by the left and right virtual walls, respectively, and A is the cross-sectional area of the simulation box perpendicular to the z direction. This gives the osmotic pressure directly from the mechanical force required to confine the solutes while allowing water to equilibrate across the virtual semipermeable boundary.

To validate the GROMACS implementation, we repeated the NaCl and KCl osmometry simulations reported by Luo and Roux.[36] The validation simulations used the same force-field description as their final optimized simulations, namely CHARMM ion parameters together with TIP3P water as modified for the CHARMM force field, including the optimized

cation–anion NBFIX parameters introduced in their work. Across the full NaCl and KCl concentration ranges reported by Luo and Roux, the osmotic pressures obtained with our flat-bottom-restraint implementation reproduced their values, confirming that the GROMACS setup gives the same osmotic pressure as the original virtual-wall approach. For the NaCl and KCl simulations, rectangular boxes were used, with dimensions of 5 nm in the x and y directions and 10 nm in the z direction. Ions were confined to the central 5 nm region along the z axis using the flat-bottomed restraints described above. For both NaCl and KCl, we simulated nominal molar concentrations of 0.1 M, 0.2 M, 0.3 M, 0.4 M, 0.5 M, 1 M, 2 M, 3 M, and 4 M, with an additional 5 M simulation for NaCl. The exact concentrations differed slightly from the nominal values because the systems contained integer numbers of ions. The corresponding molal concentrations were determined from the number of ions and the average number of water molecules between the virtual walls,[37,38] enabling direct comparison with osmotic pressures reported as a function of molal salt concentration.[42] For each NaCl and KCl system, a 5 ns NPT simulation was first performed using semi-isotropic pressure coupling with the Parrinello–Rahman barostat[65] at a reference pressure of 1 bar. Only the z dimension of the box was allowed to fluctuate, with $\tau_p = 5$ ps. The temperature was maintained at 298.15 K using the velocity-rescaling thermostat.[66] Long-range electrostatic interactions were treated using the particle-mesh Ewald method.[67] Dispersion interactions and short-range repulsion were described by a Lennard-Jones potential with a cutoff of 1 nm. Hydrogen-bond lengths were constrained using the LINCS algorithm.[68] A 2 fs integration time step was used. The final structures from the NPT simulations were used as starting structures for production simulations. Production simulations were performed in the NVT ensemble to keep the box volume fixed during osmotic-pressure calculations. All simulations used for the final reported osmotic pressures were 502 ns long. Shorter simulations were used only during parameter testing, when the osmotic pressure already showed a clear deviation from experiment; in these cases, simulations were stopped after at least 100 ns to avoid spending additional computational resources on parameter sets that were already inconsistent with

the experimental data. Ion coordinates were saved every 1 ps, and the first 2 ns of each production simulation were discarded as equilibration. Osmotic pressures were calculated from the ion coordinates at each saved frame. For the final reported 502 ns simulations, the reported values were obtained from the final 500 ns of each trajectory, and uncertainties were estimated as the standard deviation of the mean osmotic pressures calculated from five consecutive 100 ns blocks. For the shorter parameter-testing simulations, the same block-averaging procedure was applied to the available production trajectory after discarding the initial 2 ns equilibration period. We note that we were able to obtain equivalent osmotic pressure values by computing the virial pressure from the total forces (including solvent) acting on the ions, although with greater statistical uncertainty.

Residue–ion simulations were performed using the same virtual-semipermeable-wall setup as the NaCl and KCl simulations. The simulated residue–ion systems were Lys–Cl^-, Arg–Cl^-, Glu–K^+, Glu–Na^+, Asp–K^+, and Asp–Na^+. For these systems, cubic boxes were used, with dimensions of 10 nm along each of the three axes. Residues and ions were confined to the central $\sim$5 nm region of the box along the z direction. The exact width of the restrained region along z was chosen such that the nominal molar concentrations of each residue–ion system were 100 mM, 250 mM, 350 mM, and 500 mM. Throughout the manuscript, osmotic pressures are reported as a function of molal concentration. The molal concentration was determined from the number of solute particles and the average number of water molecules in the central restrained region during the production simulations. For each residue–ion system and concentration, a 25 ns NPT simulation was first performed. From each NPT simulation, five equally spaced snapshots were extracted every 5 ns and used as starting structures for five independent production simulations. Each production simulation was 252 ns long, with the first 2 ns discarded as equilibration. All other simulation parameters were identical to those used for the NaCl and KCl simulations. Osmotic pressures were calculated every 1 ps from the restrained-particle coordinates. For each residue–ion system and concentration, the reported osmotic pressure was calculated as the mean over the five independent production

simulations. Uncertainties were reported as the standard deviation across the mean osmotic pressures obtained from the five independent simulations.

Residue–residue simulations of oppositely charged pairs (Lys–Glu, Lys–Asp, Arg–Glu, and Arg–Asp) were performed using the same simulation protocol as the residue–ion systems. The only difference was the set of simulated concentrations: for each residue–residue pair, nominal molar concentrations of 200 mM, 300 mM, 400 mM, and 500 mM were used. As for the residue–ion simulations, molal concentrations were determined from the number of solute particles and the average number of water molecules in the central restrained region during the production simulations. Single-residue simulations of alanine and glycine were performed using the same setup and analysis procedure. For these systems, nominal molar concentrations of 100 mM, 250 mM, 500 mM, 1 M, and 2 M were simulated. For each residue–residue and single-residue system, a 25 ns NPT simulation was first performed, followed by five independent 252 ns production simulations initiated from five equally spaced snapshots extracted every 5 ns from the NPT trajectory. The first 2 ns of each production simulation were discarded as equilibration, and osmotic pressures were calculated every 1 ps from the restrained-particle coordinates. Reported osmotic pressures were calculated as the mean over the five independent production simulations, and uncertainties were reported as the standard deviation across the mean osmotic pressures obtained from these five simulations.

To calculate coordination numbers at near-saturation salt concentrations, we performed simulations at 6.18 mol kg^{-1} for NaCl and 4.56 mol kg^{-1} for KCl.[54] Simulations were performed in cubic boxes with a side length of 7 nm. The numbers of Na^+, K^+, and Cl^- ions were chosen such that, after replacing water molecules with ions, the target experimental molal concentrations were obtained.[54] For both NaCl and KCl, simulations were performed for the initial and all relevant modified force-field parameter sets. All simulations were at least 25 ns long, and the first 1 ns was discarded as equilibration. All other simulation parameters were identical to those used for the ion–ion osmometry simulations. Following previous work,[69] coordination numbers were determined from the Na^+–Cl^- and K^+–Cl^- radial dis-

tribution functions. The radial distribution functions were calculated using a bin width of 0.001 nm. The position of the first minimum was determined by fitting the RDF in a narrow region around the local minimum to a quadratic function, $f(r) = ar^2 + br + c$, with the minimum position calculated as $r_{\min} = -b/(2a)$. Coordination numbers were then calculated by integrating the RDF up to this first minimum, $N(r_{\min}) = 4\pi\rho \int_0^{r_{\min}} g(r) r^2 \, dr$, where ρ is the bulk number density of the counterion species, $g(r)$ is the ion–ion radial distribution function, and $r_{\min}$ is the position of the first minimum. Uncertainties were estimated using block analysis.

All-atom simulations of IDRs

All-atom simulations of the 16 dye-labeled IDRs were performed using the same solvated starting structures as in our previous work.[30] For each IDR, two sets of simulations were carried out using the osmometry-guided force-field modifications described in the main text: one using the optimized charge-scaling parameters and one using the optimized Lennard-Jones σ parameters. The previously prepared dye-labeled systems, including water and ions, were reused directly; only the force-field parameters were changed before rerunning the simulations. The starting systems contained all-atom configurations of the 16 IDR variants labeled with Cy3B and CF660R in 14 nm rhombic dodecahedral boxes with TIP4P2005s water.[18] Potassium and chloride ions were present at 172 mM KCl, matching the total ionic strength of the KCl salt and buffer used in the experiments. The total number of atoms per simulation was approximately 250,000, varying slightly among different IDRs. All simulations were performed with GROMACS version 2021.5.[64] Protein interactions were modeled using Amber99SBws,[18] together with the osmometry-guided parameter modifications described in the main text. Cy3B and CF660R were described using previously published dye parameters.[70] Dye–water Lennard-Jones interactions were scaled by a factor of 1.15 for both Cy3B and CF660R, as described previously.[71]

For simulations with the optimized charge-scaling parameters, the charges of the charged

groups within the dyes were scaled by the same factor as the charged protein residues, 0.93. For simulations with the optimized Lennard-Jones parameters, the Lennard-Jones σ parameters between the charged dye groups and water oxygen atoms were scaled by a factor of 0.99. This factor was chosen to match the average magnitude of the residue-specific σ modifications applied to charged residue–water oxygen interactions: $\sigma_{\mathrm{Lys–OW}}$ and $\sigma_{\mathrm{Asp–OW}}$ were scaled by 0.99, $\sigma_{\mathrm{Glu–OW}}$ by 0.995, and $\sigma_{\mathrm{Arg–OW}}$ by 0.985. The integration time step was 2 fs. The temperature was maintained at 295.15 K using the velocity-rescaling thermostat[66] with $\tau_t = 1\,ps$, and the pressure was maintained at 1 bar using the Parrinello–Rahman barostat[65] with $\tau_p = 5\,ps$. Long-range electrostatic interactions were treated using the particle-mesh Ewald method.[67] Dispersion interactions and short-range repulsion were described by a Lennard-Jones potential with a cutoff of 1 nm. Hydrogen-bond lengths were constrained using the LINCS algorithm.[68] Each independent simulation was at least 2.02 μs long, and the first 20 ns were discarded as equilibration.

All-atom simulations of folded–disordered complex dynamics

Simulations of the complex between the globular domain (GD) of histone H1 and ProTα were run using a protocol similar to that used previously.[56] The initial protein configuration was taken from the earlier simulations and solvated with explicit water and 165 mM potassium chloride in a 17 nm truncated-octahedral box with periodic boundary conditions. Either the original Amber ff99SBws model or the modified Amber ff99SBws-LJ model was used for the protein and ions, with TIP4P/2005 water.[46] The total number of atoms was 495,529. Simulations were performed using GROMACS 2024.1,[64] with the equations of motion integrated using the velocity-Verlet algorithm with a time step of 2 fs and LINCS constraints on all bonds. A constant temperature of 283 K was maintained using the Bussi velocity rescaling thermostat[66] with a 1 ps relaxation time, and a constant pressure of 1 atm was maintained using the Parrinello–Rahman barostat[65] with a 5 ps relaxation time. Simulations were run for 5 μs in total, with the first 3 μs discarded as equilibration.

All-atom simulations of biomolecular condensates

All-atom simulations of ProTα–H1 and ProTα–protamine condensates at 8 mM and 128 mM KCl were performed using the same system setups and simulation protocols as in our previous studies,[12,13] with the force field being the only methodological difference. The previous simulations used Amber ff99SBws, referred to as the "original force field" in the present manuscript, whereas all new simulations used Amber ff99SBws-LJ. The ProTα–H1 simulation at 128 mM KCl was initiated from the snapshot at 4 μs of the corresponding previously reported Amber ff99SBws trajectory.[12] A snapshot at 1.45 μs of the resulting Amber ff99SBws-LJ trajectory was used to initiate the ProTα–H1 simulation at 8 mM KCl. The ProTα–protamine simulation at 128 mM KCl was initiated from the same starting structure as the corresponding previously reported Amber ff99SBws simulation,[13] and a snapshot at 3.45 μs of the resulting Amber ff99SBws-LJ trajectory was used to initiate the ProTα–protamine simulation at 8 mM KCl.

All systems were simulated under periodic boundary conditions in slab geometry with TIP4P/2005s water.[46] The temperature was maintained at 295.15 K using stochastic velocity rescaling[66] with a relaxation time of 1 ps, and the pressure was maintained at 1 bar using the Parrinello–Rahman barostat.[65] Long-range electrostatic interactions were treated using the particle-mesh Ewald method[67] with a grid spacing of 0.12 nm. Lennard-Jones interactions were truncated at 0.9 nm, bonds involving hydrogen atoms were constrained using LINCS, and the equations of motion were integrated using the leap-frog algorithm with a time step of 2 fs. Simulations were performed using GROMACS version 2024.1.[64]

The ProTα–H1 simulations contained 96 ProTα and 80 H1 molecules. The system at 128 mM KCl contained 4,000,932 atoms and was simulated for 5.5 μs, with the first 1.5 μs excluded as equilibration. The system at 8 mM KCl contained 3,996,354 atoms and was simulated for 6.8 μs, with the first 1.8 μs excluded as equilibration. The ProTα–protamine simulations contained 96 ProTα and 197 protamine molecules. The system at 128 mM KCl contained 2,612,851 atoms and was simulated for 10.0 μs, with the first 2.2 μs excluded

as equilibration. The system at 8 mM KCl contained 2,609,869 atoms and was simulated for 8.4 μs, with the first 1.0 μs excluded as equilibration. Equilibration was assessed from equilibration of the protein density in the central region of the condensate slab, as described previously (Fig. S9).[12,13]

Protein mass concentrations in the dense phases (Fig. S9) were calculated from protein mass-density profiles along the z axis, as described previously.[12,13] The trajectories were divided into 50 ns blocks, and a protein mass-density profile was calculated for each block. The dense-phase concentration was obtained by averaging the profile over the central region of the condensate slab, excluding the interfacial regions. The boundaries of the central region were adjusted over the trajectory to account for changes in the position and width of the slab. For ProTα–H1 at 128 mM KCl, the following central regions were used: $21.0 < z < 37.1$ nm from 0 to 0.50 μs, $20.0 < z < 38.1$ nm from 0.50 to 1.00 μs, $19.5 < z < 37.1$ nm from 1.00 to 1.50 μs, $18.8 < z < 36.6$ nm from 1.50 to 2.10 μs, $18.8 < z < 36.8$ nm from 2.10 to 2.30 μs, $18.8 < z < 37.0$ nm from 2.30 to 2.45 μs, $19.0 < z < 37.0$ nm from 2.45 to 2.85 μs, $18.0 < z < 36.0$ nm from 2.85 to 3.05 μs, $18.3 < z < 36.3$ nm from 3.05 to 3.20 μs, $17.5 < z < 37.0$ nm from 3.20 to 3.50 μs, $18.5 < z < 37.5$ nm from 3.50 to 4.35 μs, and $18.0 < z < 38.1$ nm from 4.35 to 5.50 μs. For ProTα–H1 at 8 mM KCl, the regions were $18.5 < z < 36.5$ nm from 0 to 0.70 μs, $17.5 < z < 36.5$ nm from 0.70 to 1.40 μs, $18.5 < z < 36.1$ nm from 1.40 to 2.75 μs, $19.5 < z < 37.1$ nm from 2.75 to 4.35 μs, $20.1 < z < 36.7$ nm from 4.35 to 4.85 μs, $20.1 < z < 36.1$ nm from 4.85 to 5.50 μs, and $19.0 < z < 36.7$ nm from 5.50 to 6.80 μs. For ProTα–protamine at 128 mM KCl, the regions were $13.0 < z < 30.0$ nm from 0 to 0.10 μs, $12.0 < z < 29.0$ nm from 0.10 to 0.25 μs, $12.0 < z < 28.0$ nm from 0.25 to 0.60 μs, $13.0 < z < 27.5$ nm from 0.60 to 0.80 μs, $12.5 < z < 25.5$ nm from 0.80 to 1.00 μs, $13.0 < z < 26.5$ nm from 1.00 to 1.80 μs, $12.7 < z < 26.0$ nm from 1.80 to 6.00 μs, $12.3 < z < 25.3$ nm from 6.00 to 8.50 μs, and $13.3 < z < 25.7$ nm from 8.50 to 10.00 μs. For ProTα–protamine at 8 mM KCl, the regions were $13.0 < z < 30.0$ nm from 0 to 0.10 μs, $12.0 < z < 29.0$ nm from 0.10 to 0.25 μs, $12.0 < z < 28.0$ nm from 0.25

to 0.60 μs, $13.0 < z < 27.5$ nm from 0.60 to 0.80 μs, $12.5 < z < 25.5$ nm from 0.80 to 1.00 μs, $13.0 < z < 26.5$ nm from 1.00 to 1.80 μs, $12.7 < z < 25.5$ nm from 1.80 to 5.00 μs, $12.5 < z < 24.5$ nm from 5.00 to 6.50 μs, and $13.0 < z < 24.1$ nm from 6.50 to 8.40 μs. For each simulation, the reported protein mass concentration was calculated as the arithmetic mean of the 50 ns block values within the analyzed trajectory segment indicated in Fig. S9. Its uncertainty was taken as the standard deviation of these block values.

The transfer efficiency of ProTα was calculated as previously described.[12,13] In brief, the instantaneous transfer efficiency was calculated every 50 ps for each ProTα chain using

$$E(r) = \frac{R_0^6}{R_0^6 + r^6}, \tag{2}$$

with a Förster radius of $R_0 = 5.9$ nm. Because the fluorophores and their linkers were not represented explicitly, the interdye distance was estimated from the distance, d, between the C_α atoms of ProTα residues 58 and 112 according to

$$r = d\left(\frac{N+9}{N}\right)^{\nu}, \tag{3}$$

where N is the sequence separation between the labeling sites and $\nu = 0.6$. The additional nine effective residues account for the combined lengths of the fluorophores and their linkers. For each ProTα chain, $E(r)$ was averaged over the analyzed trajectory. The condensate-averaged mean transfer efficiency, $\langle E \rangle$, was calculated by averaging these chain-specific means over all 96 ProTα chains. The reported simulation dispersion is their standard deviation and therefore describes chain-to-chain heterogeneity rather than the uncertainty in the condensate mean.

Residue–residue contact lifetimes were calculated using a transition-based core-state approach,[72] as described previously.[12,13] In short, for each pair of residues belonging to different protein molecules, the shortest distance between any pair of heavy atoms was monitored. Contact formation was defined by this distance decreasing below 0.38 nm, whereas an ex-

isting contact was considered broken only when the distance increased above 0.8 nm. The mean lifetime of a residue–residue contact was calculated by dividing its total bound time by the number of contact-breaking events. The analysis included all intermolecular contacts involving ProTα: contacts between different ProTα molecules and between ProTα and H1 or protamine. Intrachain, H1–H1 and protamine–protamine contacts were excluded. Given the large number of included contacts, each of the four simulations performed with Amber ff99SBws-LJ was divided into blocks of 1–2 μs, and each block was analyzed independently using parallelized code. A mean contact lifetime was obtained for each block by averaging over all included contacts. For each simulation, the reported contact lifetime is the mean of the block-specific values, and its uncertainty is their standard deviation. The corresponding values for the four simulations performed with the original Amber ff99SBws force field were taken from our previous analyses, which used the same contact definition and lifetime calculation.[12,13]

Reconfiguration times were determined from the distance, $r(t)$, between the C_α atoms of residues 58 and 112 of each ProTα chain for all four simulations performed with Amber ff99SBws-LJ and the four corresponding simulations performed previously with Amber ff99SBws.[12,13] The same one-dimensional Smoluchowski diffusion model as in our previous work was used.[13] Briefly, the distance coordinate between 2 nm and 10 nm was discretized into 30 equal-width bins. For each candidate lag time, Δt, transitions from bin i to bin j were counted separately within each ProTα trajectory and subsequently pooled over the 96 chains. The discretized free energies and a constant diffusion coefficient were optimized using the previously described Monte Carlo likelihood procedure,[13,30]

$$\ln L = \sum_{i,j} N_{ji}(\Delta t) \ln \left(\exp[\Delta t \mathbf{K}]\right)_{ji}, \tag{4}$$

where $N_{ji}(\Delta t)$ is the number of observed transitions and $\mathbf{K}$ is the rate matrix constructed from the free energies and diffusion coefficient according to the discretized Smoluchowski

scheme of Bicout and Szabo.[73,74] The reconfiguration time was calculated from the eigenvalues, λ_n, and right eigenvectors, $\mathbf{\Psi}_n^R$, of $\mathbf{K}$ as

$$\tau_c = -\frac{\sum_{n=2}^{b} \left(\mathbf{r} \cdot \mathbf{\Psi}_n^R\right)^2 \lambda_n^{-1}}{\sum_{n=2}^{b} \left(\mathbf{r} \cdot \mathbf{\Psi}_n^R\right)^2}, \tag{5}$$

where the elements of $\mathbf{r}$ are the centers of the distance bins.

In our previous analysis,[13] a common lag time of 200 ns was used for all systems based on the apparent convergence of τ_c with lag time, and the values obtained at 100 ns and 300 ns were used to estimate the associated lag-choice uncertainty. Several of the new trajectories are substantially longer than those analyzed previously, allowing a more stringent assessment of lag dependence. We therefore reanalyzed all eight trajectories using a system-specific predictive criterion rather than imposing the same lag time on every system. The lag used to define the lag-time averaging window was selected using a Chapman–Kolmogorov (CK) predictive test.[75] For each candidate lag, the fitted rate matrix was propagated to $2\Delta t$, $3\Delta t$, and $4\Delta t$, and the resulting model transition matrices were compared with empirical transition matrices counted directly from the trajectories at the corresponding longer lag times. At each prediction time, the discrepancy was quantified using a population-weighted total-variation distance,

$$d_m = \sum_i w_i \frac{1}{2} \sum_j \left| T_{ji}^{\mathrm{emp}}(m\Delta t) - T_{ji}^{\mathrm{model}}(m\Delta t) \right|, \qquad m = 2, 3, 4, \tag{6}$$

where the origin bins were weighted by their observed populations, w_i.

To determine the magnitude of the discrepancy expected from finite sampling alone, complete ProTα trajectories were resampled with replacement. Each bootstrap replicate contained 96 trajectories drawn from the original set of 96 ProTα trajectories, thereby preserving the temporal correlations within each trajectory. For every bootstrap replicate,

empirical transition matrices were recalculated at $2\Delta t$, $3\Delta t$, and $4\Delta t$, and their population-weighted total-variation distances from the corresponding full-data empirical matrices were determined. The 95th percentile of this bootstrap distribution, $q_{95,m}^{\mathrm{boot}}$, defined the finite-sampling noise threshold at each prediction time. Only prediction times retaining at least 200 estimated independent transitions were included. The CK score was calculated as

$$S_{\mathrm{CK}} = \max_{m=2,3,4} \frac{d_m}{q_{95,m}^{\mathrm{boot}}}. \tag{7}$$

A CK-score acceptance criterion of $S_{\mathrm{CK}} \leq 1$ was used; values of $S_{\mathrm{CK}} > 1$ were therefore classified as not passing the CK test. The smallest lag that passed the CK test was selected as the reference lag. For passing cases, the reported τ_c was the unweighted mean over all CK-passing candidate lags, and the sample standard deviation of τ_c across these lags was reported as a descriptive measure of its lag dependence. If no candidate lag passed the CK test, the lag with the lowest CK score was selected as the reference lag, and the result was reported as a best-effort, not-converged estimate. The averaging set in these cases comprised the selected lag and adjacent, sufficiently sampled candidate lags with CK scores no more than 25% above the minimum score. The reported τ_c was again the unweighted mean over this lag set, with its sample standard deviation reported as the lag-dependence uncertainty.

As a control for the CK-based analysis, we applied the same procedure to interdye-distance trajectories from 15 independent all-atom simulations of the explicitly dye-labeled disordered peptide G(AGQ)$_6$AGC, each approximately 1.1 μs long.[71] The CK test passed at a reference lag of 3.5 ns, and the CK-passing candidate lags used for averaging were 3.5, 4, 4.5, 5, 6, 7, 8, 9, 10, 12, 14, 15, 20, 25 and 50 ns, yielding a reconfiguration time of (14 ± 2) ns. This value agrees with the previously reported values of 15 ns from direct autocorrelation of the MD interdye distance and 14 ns from a one-dimensional diffusion analysis based on simulated photon-emission data.[71]

For the ProTα–H1 condensate at 128 mM KCl, the CK test passed for both force fields.

With Amber ff99SBws, the reference lag was 625 ns, and the CK-passing candidate lags used for averaging were 625, 750, 875, and 1000 ns. With Amber ff99SBws-LJ, the reference lag was 500 ns, and the CK-passing candidate lags used for averaging were 500, 600, 700, 800, and 900 ns.

For the ProTα–H1 condensate at 8 mM KCl, no candidate lag passed the CK test for Amber ff99SBws. The lowest CK score was 1.2 at a reference lag of 200 ns, and the local lag set used for averaging comprised 100 and 200 ns. For Amber ff99SBws-LJ, the CK test passed, the reference lag was 700 ns, and the CK-passing candidate lags used for averaging were 700, 800, 825, 850, 900, 950, 975, and 1000 ns. The analyzed part of the Amber ff99SBws trajectory was substantially shorter than that of the Amber ff99SBws-LJ trajectory, 1 μs compared with 5 μs, respectively. The Amber ff99SBws reconfiguration time shown in Fig. 5 should therefore be interpreted as a likely underestimate.

For the ProTα–protamine condensate at 128 mM KCl, no candidate lag passed the CK test for either force field. For Amber ff99SBws, the lowest CK score was 1.5 at a reference lag of 200 ns, and the local lag set used for averaging comprised 50, 100, 150, and 200 ns. For Amber ff99SBws-LJ, the lowest CK score was $S_{\mathrm{CK}} = 1.001$ at a reference lag of 1000 ns. Although this value nominally failed the acceptance criterion, it exceeded the threshold by only 0.1%, indicating that the fitted model came very close to reproducing the longer-lag transition matrices within the bootstrap-estimated finite-sampling uncertainty. The result was nevertheless treated conservatively as a best-effort, not-converged estimate, and the local lag set used for averaging comprised 700, 800, and 1000 ns. The analyzed part of the Amber ff99SBws trajectory was substantially shorter than that of the Amber ff99SBws-LJ trajectory, 1.1 μs compared with 7.8 μs, respectively. The Amber ff99SBws reconfiguration time shown in Fig. reffigcond should therefore be interpreted as a likely underestimate.

For the ProTα–protamine condensate at 8 mM KCl, no candidate lag passed the CK test with either force field. For Amber ff99SBws, the lowest CK score was 1.5 at a reference lag of 300 ns, and the local lag set used for averaging comprised 200 and 300 ns. For Am-

ber ff99SBws-LJ, the lowest CK score was 1.2 at a reference lag of 1500 ns, and the local lag set used for averaging comprised 1000 and 1500 ns. The analyzed part of the Amber ff99SBws trajectory was substantially shorter than that of the Amber ff99SBws-LJ trajectory, 1.3 μs compared with 7.4 μs, respectively. The Amber ff99SBws reconfiguration time shown in Fig. 5 should therefore be interpreted as a likely underestimate.

Importantly, irrespective of the exact choice of lag time, Amber ff99SBws-LJ agrees with the experimental reconfiguration times substantially better than Amber ff99SBws (Fig. S10).

Data availability

The experimental osmometry data, numerical source data underlying the figures and tables, and optimized force-field parameter files obtained in this study are publicly available from Zenodo at `https://doi.org/10.5281/zenodo.20031526`.

Acknowledgement

We thank Gerhard Hummer, Aritra Chowdhury and Rohan Eapen for insightful discussions, Annette Bieger Altermatt and Hille Ris for access to the osmometer and helpful discussions, Andrea Sottini for guidance on sample preparation and David Wang for helpful comments on the manuscript. The work was supported by the Novo Nordisk Foundation (#NNF18OC0033926 to B.S.) and the Swiss National Science Foundation (grant number 10006187). We used the computational resources of Alps, Piz Daint and Eiger at the CSCS Swiss National Supercomputing Center, and of the National Institutes of Health HPC Biowulf cluster (http://hpc.nih.gov).

References

(1) Holehouse, A. S.; Kragelund, B. B. The molecular basis for cellular function of intrinsically disordered protein regions. *Nat. Rev. Mol. Cell Biol.* **2024**, *25*, 187–211.

(2) Schuler, B.; Borgia, A.; Borgia, M. B.; Heidarsson, P. O.; Holmstrom, E. D.; Nettels, D.; Sottini, A. Binding without folding - the biomolecular function of disordered polyelectrolyte complexes. *Curr. Opin. Struct. Biol.* **2020**, *60*, 66–76.

(3) Borgia, A.; Borgia, M. B.; Bugge, K.; Kissling, V. M.; Heidarsson, P. O.; Fernandes, C. B.; Sottini, A.; Soranno, A.; Buholzer, K. J.; Nettels, D.; others Extreme disorder in an ultrahigh-affinity protein complex. *Nature* **2018**, *555*, 61–66.

(4) Banani, S. F.; Lee, H. O.; Hyman, A. A.; Rosen, M. K. Biomolecular condensates: organizers of cellular biochemistry. *Nat. Rev. Mol. Cell Biol.* **2017**, *18*, 285–298.

(5) Brangwynne, C. P.; Eckmann, C. R.; Courson, D. S.; Rybarska, A.; Hoege, C.; Gharakhani, J.; Jülicher, F.; Hyman, A. A. Germline P granules are liquid droplets that localize by controlled dissolution/condensation. *Science* **2009**, *324*, 1729–1732.

(6) Cramer, P. Organization and regulation of gene transcription. *Nature* **2019**, *573*, 45–54.

(7) Bottaro, S.; Lindorff-Larsen, K. Biophysical experiments and biomolecular simulations: A perfect match? *Science* **2018**, *361*, 355–360.

(8) Alberti, S.; Arosio, P.; Best, R. B.; Boeynaems, S.; Cai, D.; Collepardo-Guevara, R.; Dignon, G. L.; Dimova, R.; Elbaum-Garfinkle, S.; Fawzi, N. L.; others Current practices in the study of biomolecular condensates: a community comment. *Nat. Commun.* **2025**, *16*, 7730.

(9) Dignon, G. L.; Zheng, W.; Kim, Y. C.; Best, R. B.; Mittal, J. Sequence determinants of protein phase behavior from a coarse-grained model. *PLoS Comput. Biol.* **2018**, *14*, e1005941.

(10) Alshareedah, I.; Borcherds, W. M.; Cohen, S. R.; Singh, A.; Posey, A. E.; Farag, M.; Bremer, A.; Strout, G. W.; Tomares, D. T.; Pappu, R. V.; others Sequence-specific interactions determine viscoelasticity and ageing dynamics of protein condensates. *Nat. Phys.* **2024**, *20*, 1482–1491.

(11) Schäfer, L. V.; Stelzl, L. S. Deciphering driving forces of biomolecular phase separation from simulations. *Curr. Opin. Struct. Biol.* **2025**, *92*, 103026.

(12) Galvanetto, N.; Ivanović, M. T.; Chowdhury, A.; Sottini, A.; Nüesch, M. F.; Nettels, D.; Best, R. B.; Schuler, B. Extreme dynamics in a biomolecular condensate. *Nature* **2023**, *619*, 876–883.

(13) Galvanetto, N.; Ivanović, M. T.; Del Grosso, S. A.; Chowdhury, A.; Sottini, A.; Nettels, D.; Best, R. B.; Schuler, B. Material properties of biomolecular condensates emerge from nanoscale dynamics. *Proc. Natl. Acad. Sci. U.S.A.* **2025**, *122*, e2424135122.

(14) Ivanović, M. T.; Best, R. B. All-atom simulations of biomolecular condensates. *Curr. Opin. Struct. Biol.* **2025**, *93*, 103101.

(15) Best, R. B.; Hummer, G. Optimized molecular dynamics force fields applied to the helix- coil transition of polypeptides. *J. Phys. Chem. B* **2009**, *113*, 9004–9015.

(16) Best, R. B.; Zhu, X.; Shim, J.; Lopes, P. E.; Mittal, J.; Feig, M.; MacKerell Jr, A. D. Optimization of the additive CHARMM all-atom protein force field targeting improved sampling of the backbone ϕ, ψ and side-chain $\chi1$ and $\chi2$ dihedral angles. *J. Chem. Theory Comput.* **2012**, *8*, 3257–3273.

(17) Shi, Y.; Xia, Z.; Zhang, J.; Best, R.; Wu, C.; Ponder, J. W.; Ren, P. Polarizable atomic multipole-based AMOEBA force field for proteins. *J. Chem. Theory Comput.* **2013**, *9*, 4046–4063.

(18) Best, R. B.; Zheng, W.; Mittal, J. Balanced protein–water interactions improve properties of disordered proteins and non-specific protein association. *J. Chem. Theory Comput.* **2014**, *10*, 5113–5124.

(19) Piana, S.; Donchev, A. G.; Robustelli, P.; Shaw, D. E. Water dispersion interactions strongly influence simulated structural properties of disordered protein states. *J. Phys. Chem. B* **2015**, *119*, 5113–5123.

(20) Huang, J.; Rauscher, S.; Nawrocki, G.; Ran, T.; Feig, M.; De Groot, B. L.; Grubmüller, H.; MacKerell Jr, A. D. CHARMM36m: an improved force field for folded and intrinsically disordered proteins. *Nat. Methods* **2017**, *14*, 71–73.

(21) Robustelli, P.; Piana, S.; Shaw, D. E. Developing a molecular dynamics force field for both folded and disordered protein states. *Proc. Natl. Acad. Sci. U.S.A.* **2018**, *115*, E4758–E4766.

(22) Piana, S.; Robustelli, P.; Tan, D.; Chen, S.; Shaw, D. E. Development of a force field for the simulation of single-chain proteins and protein–protein complexes. *J. Chem. Theory Comput.* **2020**, *16*, 2494–2507.

(23) Lin, F.-Y.; Huang, J.; Pandey, P.; Rupakheti, C.; Li, J.; Roux, B.; MacKerell Jr, A. D. Further optimization and validation of the classical Drude polarizable protein force field. *J. Chem. Theory Comput.* **2020**, *16*, 3221–3239.

(24) Lindorff-Larsen, K.; Piana, S.; Dror, R. O.; Shaw, D. E. How fast-folding proteins fold. *Science* **2011**, *334*, 517–520.

(25) Henriques, J.; Cragnell, C.; Skepo, M. Molecular dynamics simulations of intrinsically disordered proteins: force field evaluation and comparison with experiment. *J. Chem. Theory Comput.* **2015**, *11*, 3420–3431.

(26) Shrestha, U. R.; Juneja, P.; Zhang, Q.; Gurumoorthy, V.; Borreguero, J. M.; Urban, V.; Cheng, X.; Pingali, S. V.; Smith, J. C.; O'Neill, H. M.; others Generation of the configurational ensemble of an intrinsically disordered protein from unbiased molecular dynamics simulation. *Proc. Natl. Acad. Sci. U.S.A.* **2019**, *116*, 20446–20452.

(27) Ahmed, M. C.; Papaleo, E.; Lindorff-Larsen, K. How well do force fields capture the strength of salt bridges in proteins? *PeerJ* **2018**, *6*, e4967.

(28) Mason, P. E.; Jungwirth, P.; Duboué-Dijon, E. Quantifying the strength of a salt bridge by neutron scattering and molecular dynamics. *J. Phys. Chem. Lett.* **2019**, *10*, 3254–3259.

(29) Debiec, K. T.; Gronenborn, A. M.; Chong, L. T. Evaluating the strength of salt bridges: a comparison of current biomolecular force fields. *J. Phys. Chem. B* **2014**, *118*, 6561–6569.

(30) Ivanovic, M. T.; Holla, A.; Nuesch, M. F.; Von Roten, V.; Schuler, B.; Best, R. B. Dynamical Buffering of Reconfiguration Dynamics in Intrinsically Disordered Proteins. *JACS Au* **2026**, *6*, 1900–1913.

(31) Lu, X.; Chen, J.; Huang, J. The continuous evolution of biomolecular force fields. *Structure* **2025**, *33*, 1138–1149.

(32) Leontyev, I.; Stuchebrukhov, A. Electronic continuum model for molecular dynamics simulations. *J. Chem. Phys.* **2009**, *130*.

(33) Kirby, B. J.; Jungwirth, P. Charge scaling manifesto: A way of reconciling the inherently macroscopic and microscopic natures of molecular simulations. *J. Phys. Chem. Lett.* **2019**, *10*, 7531–7536.

(34) Blazquez, S.; Conde, M.; Vega, C. Scaled charges for ions: An improvement but not the final word for modeling electrolytes in water. *J. Chem. Phys.* **2023**, *158*.

(35) Nencini, R.; Tempra, C.; Biriukov, D.; Riopedre-Fernandez, M.; Cruces Chamorro, V.; Polák, J.; Mason, P. E.; Ondo, D.; Heyda, J.; Ollila, O. S.; others Effective inclusion of electronic polarization improves the description of electrostatic interactions: The prosECCo75 biomolecular force field. *J. Chem. Theory Comput.* **2024**, *20*, 7546–7559.

(36) Luo, Y.; Roux, B. Simulation of osmotic pressure in concentrated aqueous salt solutions. *J. Phys. Chem. Lett.* **2010**, *1*, 183–189.

(37) Miller, M. S.; Lay, W. K.; Elcock, A. H. Osmotic pressure simulations of amino acids and peptides highlight potential routes to protein force field parameterization. *J. Phys. Chem. B* **2016**, *120*, 8217–8229.

(38) Miller, M. S.; Lay, W. K.; Li, S.; Hacker, W. C.; An, J.; Ren, J.; Elcock, A. H. Reparametrization of protein force field nonbonded interactions guided by osmotic coefficient measurements from molecular dynamics simulations. *J. Chem. Theory Comput.* **2017**, *13*, 1812–1826.

(39) Hagler, A.; Huler, E.; Lifson, S. Energy functions for peptides and proteins. I. Derivation of a consistent force field including the hydrogen bond from amide crystals. *J. Am. Chem. Soc.* **1974**, *96*, 5319–5327.

(40) Bonner, O. D. Osmotic and activity coefficients of sodium and potassium glutamate at 298.15 K. *J. Chem. Eng. Data* **1981**, *26*, 147–148.

(41) Bonner, O. D. Osmotic and activity coefficients of some amino acids and their hydrochloride salts at 298.15 K. *J. Chem. Eng. Data* **1982**, *27*, 422–423.

(42) Robinson, R. A.; Stokes, R. H. *Electrolyte solutions*; Courier Corporation, 2002.

(43) Fisher, R. S.; Elbaum-Garfinkle, S. Tunable multiphase dynamics of arginine and lysine liquid condensates. *Nat. Commun.* **2020**, *11*, 4628.

(44) Schuster, B. S.; Dignon, G. L.; Tang, W. S.; Kelley, F. M.; Ranganath, A. K.; Jahnke, C. N.; Simpkins, A. G.; Regy, R. M.; Hammer, D. A.; Good, M. C.; others Identifying sequence perturbations to an intrinsically disordered protein that determine its phase-separation behavior. *Proc. Natl. Acad. Sci. U.S.A.* **2020**, *117*, 11421–11431.

(45) von Roten, V.; Ivanović, M. T.; Gopi, S.; Holla, A.; Prestel, A.; Nüesch, M.; Tamburrini, K. C.; Nettels, D.; Kragelund, B. B.; Best, R. B.; others Cooperativity, dynamics, and the free-energy surfaces of charge-patterned IDPs. *bioRxiv* **2026**, 2026–05.

(46) Abascal, J. L.; Vega, C. A general purpose model for the condensed phases of water: TIP4P/2005. *J. Chem. Phys.* **2005**, *123*.

(47) Smith, P. K.; Smith, E. R. Thermodynamic properties of solutions of amino acids and related substances: II. The activity of aliphatic amino acids in aqueous solution at twenty-five degrees. *J. Biol. Chem.* **1937**, *121*, 607–613.

(48) Smith, E. R.; Smith, P. K. Thermodynamic Properties of Solutions of Amino Acids and Related Substances: VI. The Activities of Some Peptides in Aqueous Solution at Twenty-Five Degrees. *J. Biol. Chem.* **1940**, *135*, 273–279.

(49) Kann, Z.; Skinner, J. A scaled-ionic-charge simulation model that reproduces enhanced and suppressed water diffusion in aqueous salt solutions. *J. Chem. Phys.* **2014**, *141*.

(50) Fuentes-Azcatl, R.; Barbosa, M. C. Sodium chloride, NaCl/: New force field. *J. Phys. Chem. B.* **2016**, *120*, 2460–2470.

(51) Duboué-Dijon, E.; Mason, P. E.; Fischer, H. E.; Jungwirth, P. Hydration and ion pairing in aqueous Mg2+ and Zn2+ solutions: force-field description aided by neutron scattering experiments and ab initio molecular dynamics simulations. *J. Phys. Chem. B* **2017**, *122*, 3296–3306.

(52) Duboue-Dijon, E.; Javanainen, M.; Delcroix, P.; Jungwirth, P.; Martinez-Seara, H. A practical guide to biologically relevant molecular simulations with charge scaling for electronic polarization. *J. Chem. Phys.* **2020**, *153*.

(53) Marcus, Y. Thermodynamics of solvation of ions. Part 5.—Gibbs free energy of hydration at 298.15 K. *J. Chem. Soc., Faraday Trans.* **1991**, *87*, 2995–2999.

(54) Ohtaki, H.; Fukushima, N. A structural study of saturated aqueous solutions of some alkali halides by X-ray diffraction. *J. Solut. Chem.* **1992**, *21*, 23–38.

(55) Holla, A.; Martin, E. W.; Dannenhoffer-Lafage, T.; Ruff, K. M.; Konig, S. L.; Nuesch, M. F.; Chowdhury, A.; Louis, J. M.; Soranno, A.; Nettels, D.; others Identifying sequence effects on chain dimensions of disordered proteins by integrating experiments and simulations. *JACS Au* **2024**, *4*, 4729–4743.

(56) Bugge, K.; Sottini, A.; Ivanović, M. T.; Buus, F. S.; Saar, D.; Fernandes, C. B.; Kocher, F.; Martinsen, J. H.; Schuler, B.; Best, R. B.; others Role of charges in a dynamic disordered complex between an IDP and a folded domain. *Nat. Commun.* **2025**, *16*, 3242.

(57) Sabari, B. R.; Dall'Agnese, A.; Boija, A.; Klein, I. A.; Coffey, E. L.; Shrinivas, K.; Abraham, B. J.; Hannett, N. M.; Zamudio, A. V.; Manteiga, J. C.; others Coactivator condensation at super-enhancers links phase separation and gene control. *Science* **2018**, *361*, eaar3958.

(58) Shin, Y.; Chang, Y.-C.; Lee, D. S.; Berry, J.; Sanders, D. W.; Ronceray, P.; Wingreen, N. S.; Haataja, M.; Brangwynne, C. P. Liquid nuclear condensates mechanically sense and restructure the genome. *Cell* **2018**, *175*, 1481–1491.

(59) Yoo, J.; Aksimentiev, A. Improved parameterization of amine–carboxylate and amine–phosphate interactions for molecular dynamics simulations using the CHARMM and AMBER force fields. *J. Chem. Theory Comput.* **2016**, *12*, 430–443.

(60) Cornell, W. D.; Cieplak, P.; Bayly, C. I.; Gould, I. R.; Merz, K. M.; Ferguson, D. M.; Spellmeyer, D. C.; Fox, T.; Caldwell, J. W.; Kollman, P. A. A second generation force field for the simulation of proteins, nucleic acids, and organic molecules. *J. Am. Chem. Soc.* **1995**, *117*, 5179–5197.

(61) Best, R. B.; de Sancho, D.; Mittal, J. Residue-specific α-helix propensities from molecular simulation. *Biophys. J.* **2012**, *102*, 1462–1467.

(62) Bayly, C. I.; Cieplak, P.; Cornell, W.; Kollman, P. A. A well-behaved electrostatic potential based method using charge restraints for deriving atomic charges: the RESP model. *J. Phys. Chem.* **1993**, *97*, 10269–10280.

(63) Frisch, M.; Trucks, G.; Schlegel, H.; Scuseria, G.; Robb, M.; Cheeseman, J.; Scalmani, G.; Barone, V.; Petersson, G.; Nakatsuji, H.; others Gaussian 16 Revision C. 01. 2016; Gaussian Inc. *Wallingford CT* **2016**, *421*.

(64) Abraham, M. J.; Murtola, T.; Schulz, R.; Páll, S.; Smith, J. C.; Hess, B.; Lindahl, E. GROMACS: High performance molecular simulations through multi-level parallelism from laptops to supercomputers. *SoftwareX* **2015**, *1*, 19–25.

(65) Parrinello, M.; Rahman, A. Polymorphic transitions in single crystals: A new molecular dynamics method. *J. Appl. Phys.* **1981**, *52*, 7182–7190.

(66) Bussi, G.; Donadio, D.; Parrinello, M. Canonical sampling through velocity rescaling. *J. Chem. Phys.* **2007**, *126*.

(67) Darden, T.; York, D.; Pedersen, L.; others Particle mesh Ewald: An N log (N) method for Ewald sums in large systems. *J. Chem. Phys.* **1993**, *98*, 10089–10092.

(68) Hess, B.; Bekker, H.; Berendsen, H. J.; Fraaije, J. G. LINCS: A linear constraint solver for molecular simulations. *J. Comput. Chem.* **1997**, *18*, 1463–1472.

(69) Satarifard, V.; Kashefolgheta, S.; Vila Verde, A.; Grafmuller, A. Is the solution activity derivative sufficient to parametrize ion–ion interactions? Ions for tip5p water. *J. Chem. Theory Comput.* **2017**, *13*, 2112–2122.

(70) Best, R. B.; Hofmann, H.; Nettels, D.; Schuler, B. Quantitative interpretation of FRET experiments via molecular simulation: force field and validation. *Biophys. J.* **2015**, *108*, 2721–2731.

(71) Nüesch, M.; Ivanović, M. T.; Nettels, D.; Best, R. B.; Schuler, B. Accuracy of distance distributions and dynamics from single-molecule FRET. *Biophys. J.* **2025**,

(72) Best, R. B.; Hummer, G.; Eaton, W. A. Native contacts determine protein folding mechanisms in atomistic simulations. *Proc. Natl. Acad. Sci. U.S.A.* **2013**, *110*, 17874–17879.

(73) Hummer, G. Position-dependent diffusion coefficients and free energies from Bayesian analysis of equilibrium and replica molecular dynamics simulations. *New J. Phys.* **2005**, *7*, 34–34.

(74) Bicout, D.; Szabo, A. Electron transfer reaction dynamics in non-Debye solvents. *J. Chem. Phys.* **1998**, *109*, 2325–2338.

(75) Prinz, J.-H.; Wu, H.; Sarich, M.; Keller, B.; Senne, M.; Held, M.; Chodera, J. D.; Schütte, C.; Noé, F. Markov models of molecular kinetics: Generation and validation. *J. Chem. Phys.* **2011**, *134*.

Supplementary Information for: Predictive all-atom simulations of disordered proteins and biomolecular condensates through osmometry-guided force-field optimization

Miloš T. Ivanović,[*,†] Valentin von Roten,[†] Benjamin Schuler,[*,‡] and Robert B. Best[*,¶]

†*Department of Biochemistry, University of Zurich, Winterthurerstrasse 190, 8057 Zurich, Switzerland*

‡*Department of Biochemistry and Department of Physics, University of Zurich, Winterthurerstrasse 190, 8057 Zurich, Switzerland*

¶*Laboratory of Chemical Physics, National Institute of Diabetes and Digestive and Kidney Diseases, National Institutes of Health, Bethesda, MD, 20892-0520, U.S.A.*

E-mail: m.ivanovic@bioc.uzh.ch; schuler@bioc.uzh.ch; robert.best2@nih.gov

Supporting Figures

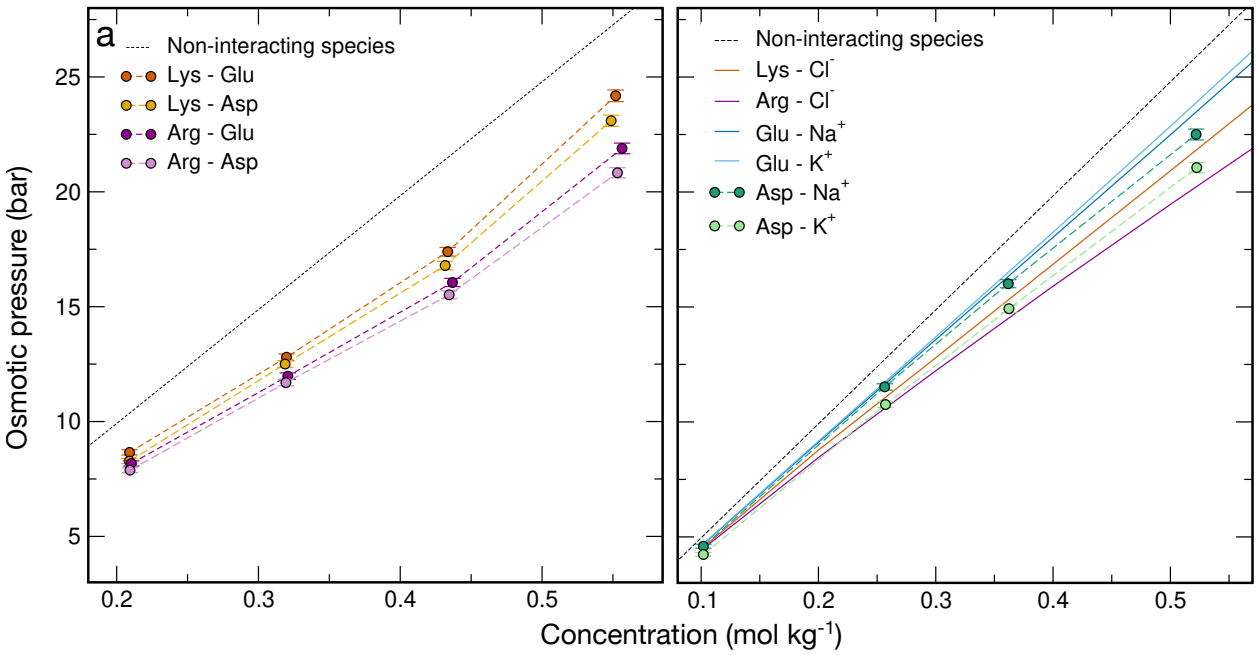

Figure S1: Experimental osmotic pressure values. (a) Residue–residue interactions; (b) residue–ion interactions. Theoretical osmotic pressures for pairs of non-interacting species are shown versus molal concentration as black dotted lines. All measured osmotic pressures lie below the corresponding non-interacting values, consistent with predominantly attractive interactions in these solutions of oppositely charged species.

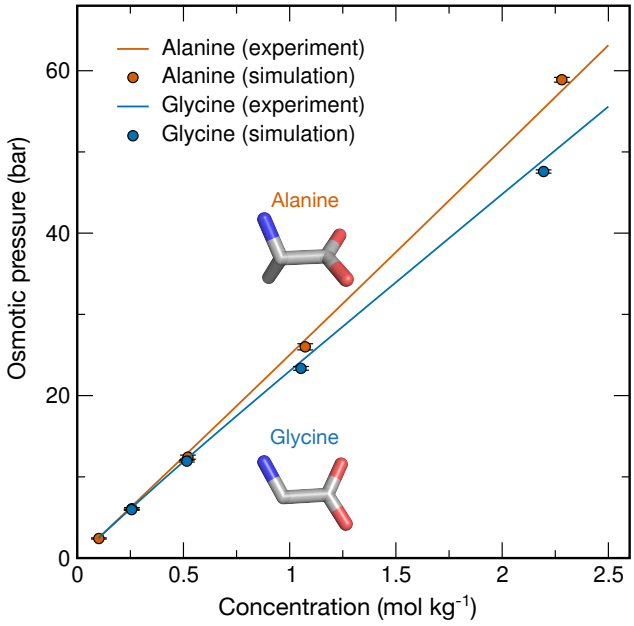

Figure S2: Zwitterionic parameter validation. Experimental osmotic pressures (solid lines) and osmotic pressures calculated from simulations of Alanine and Glycine in their zwitterionic forms (filled circles).

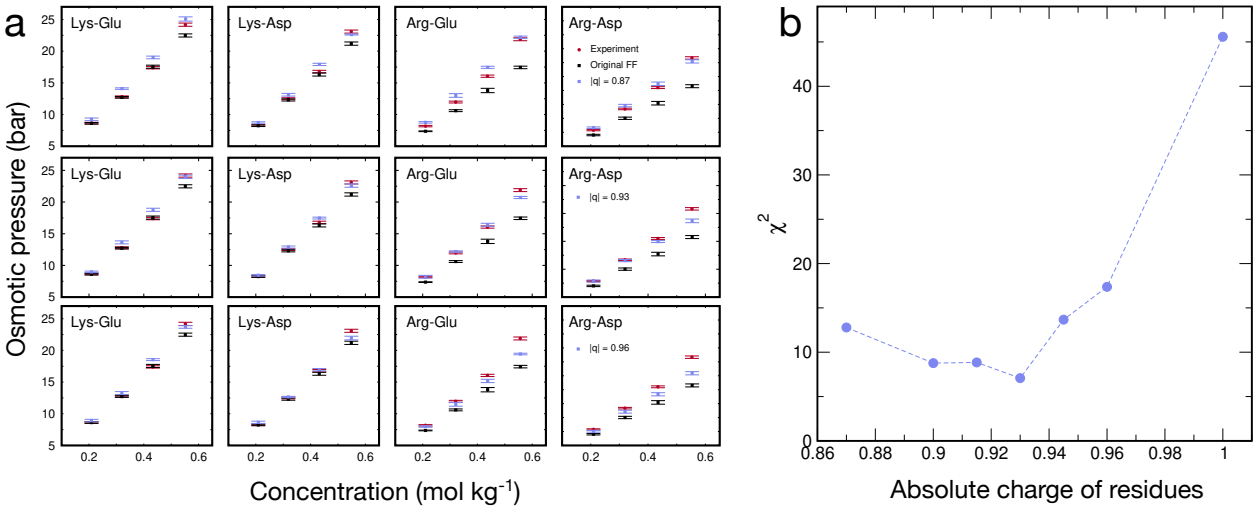

Figure S3: Amber ff99SBws-CS: Determining absolute charge of residues. We assumed that the absolute charge of all charged residues is scaled to the same value. (a) Osmotic pressure of four sets of simulations (columns: Lys-Glu, Lys-Asp, Arg-Glu and Arg-Asp) each at four different amino acid concentrations, and their comparison to the experiment. Examples are shown for the absolute charges scaled to $\pm$ 0.87 (top row), $\pm$ 0.93 (middle row) and $\pm$ 0.96 (bottom row). (b) Overall agreement with experimental osmotic pressure data as a function of selected absolute charge, expressed using the unreduced χ^2 parameter.

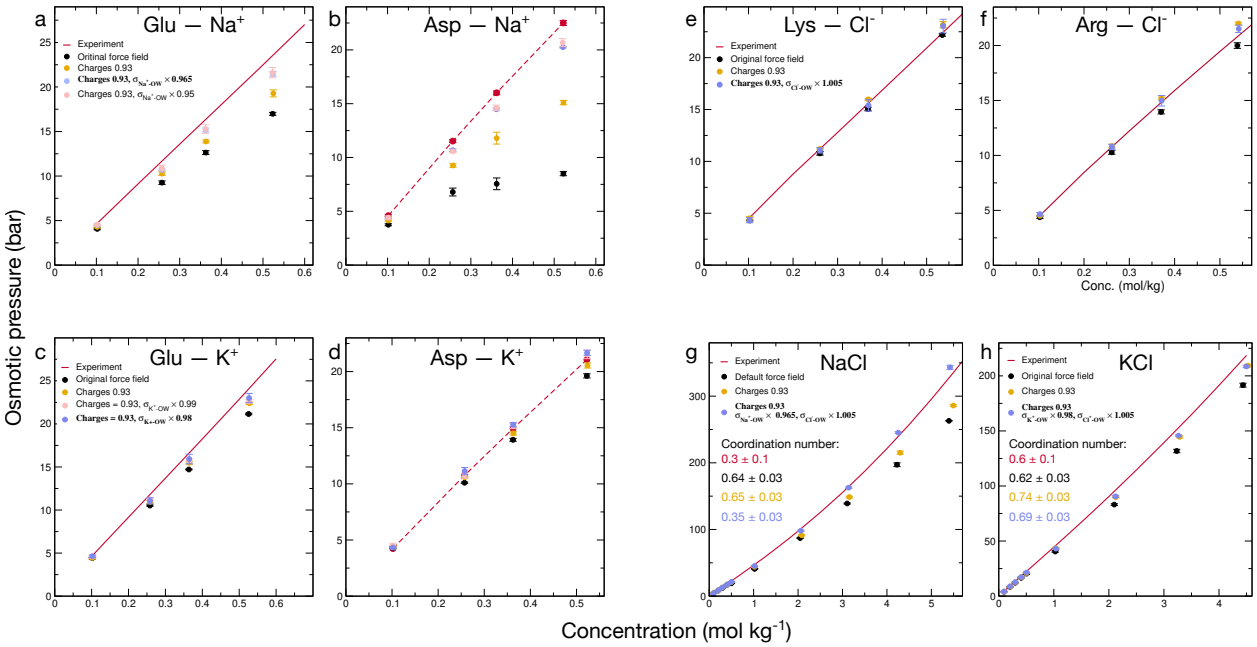

Figure S4: Amber ff99SBws-CS optimization: Optimizing protein-ion and ion-ion interactions after scaling the charges. Glu–Na^+ and Asp–Na^+ interactions are too strong with the original force field, which is a common feature of many force-fields.[1–3] K^+–Cl^- interactions are also slightly too strong.[3] As evident from the graphs a and b, reducing the charges of Glu and Na residues to -0.93 and Na^+ to +0.93, the osmotic pressure increases to be closer to experiment, but the interactions are still too strong. To better match the experimental data, the Lennard-Jones σ parameter between the ions and water oxygen (OW) was tuned as noted in the figure legends. In g and h, the coordination number is shown for the experiment and each set of simulation parameters inside the graph. The final parameter set is highlighted in bold in each panel.

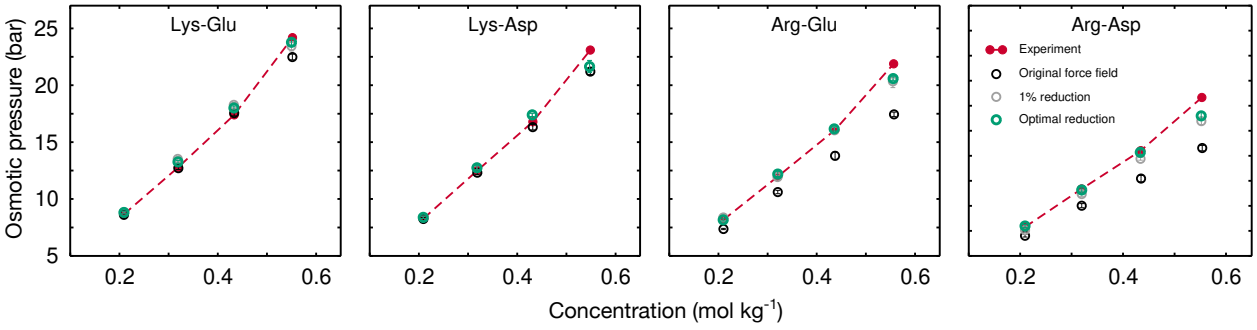

Figure S5: Amber ff99SBws-LJ optimization: effect of reducing the side-chain–OW Lennard-Jones σ parameters on the osmotic pressures of residue–residue mixtures. Experimental osmotic pressures (red circles and dashed lines) are compared with simulations using Amber ff99SBws (black circles), a uniform 1% reduction of the side-chain–OW σ parameters for all four charged residues (gray circles), and optimized residue-specific reductions (green circles). The corresponding optimized scaling factors are 0.99 for $\sigma_{\text{Lys–OW}}$, 0.985 for $\sigma_{\text{Arg–OW}}$, 0.995 for $\sigma_{\text{Glu–OW}}$, and 0.99 for $\sigma_{\text{Asp–OW}}$.

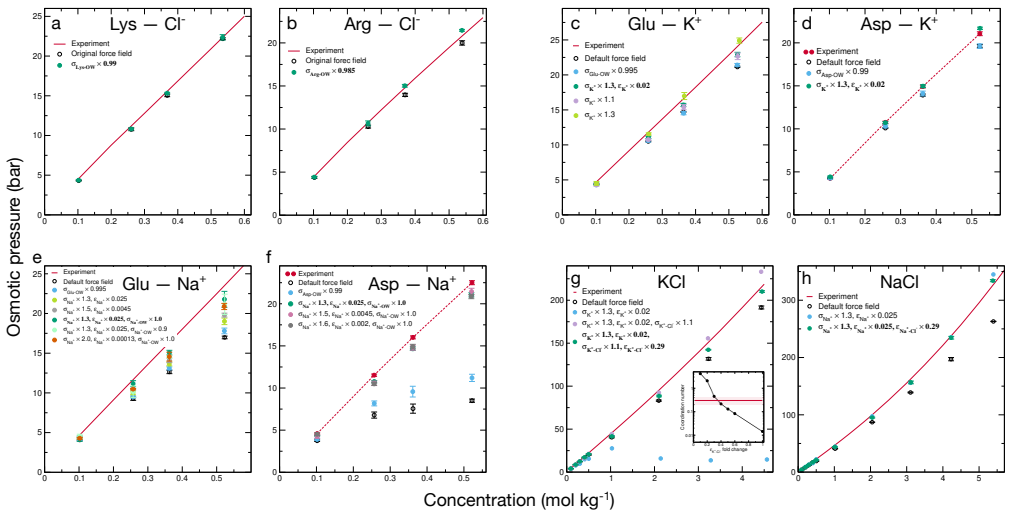

Figure S6: Amber ff99SBws-LJ: protein–ion and ion–ion parameters. (a,b) Lys/Arg–Cl^- interactions: experimental osmotic pressure (red), osmotic pressure calculated from simulations using the default force field (black), and osmotic pressure after Lys/Arg–OW interactions have been modified (green). (c,d) Glu/Asp–K^+ interactions: experimental osmotic pressure (red), osmotic pressure calculated from simulations using the default force field (black), and osmotic pressure after Glu/Asp–OW interactions have been modified (light blue). Because Glu/Asp–K^+ interactions remained too strong after Glu/Asp–OW modifications, we further adjusted the K^+ Lennard-Jones σ and ϵ such that the effective radius of K^+ remained unchanged. The final modification, with K^+ σ increased by a factor of 1.3 and K^+ ϵ scaled by a factor of 0.02 (dark green), provides a compromise that on average describes both Glu–K^+ and Asp–K^+ interactions well. The effect of changing σ can be seen by comparing the light blue, purple, and light green symbols in panel (c), whereas the effect of changing ϵ can be seen by comparing the light green and dark green symbols in panel (c). Note that for the dark green, light green, and purple symbols, Glu–OW σ was also modified by a factor of 0.995, as explicitly indicated only in the light blue symbol legend. (e,f) Glu/Asp–Na^+ interactions: experimental osmotic pressure (red), osmotic pressure calculated from simulations using the default force field (black), and osmotic pressure after Glu/Asp–OW interactions have been modified (light blue). Note that for all symbols listed below the light blue entry in the legend, Glu/Asp–OW interactions have been modified as described in the main text and in Fig. S5 (reducing Glu–OW σ by 0.5% and Asp–OW σ by 1%). As apparent from panels (e) and (f), increasing the Na^+ σ improves agreement with experiment, but this improvement nearly saturates when σ has been increased by a factor of 1.3. The maximal improvement is obtained for a Na^+–OW σ value corresponding to the Na^+–OW σ of the unmodified ion (i.e., the value before Na^+ σ and ϵ were changed, denoted by Na-OW σ 1.0). Further modifications of Na^+–OW σ do not lead to any noticeable improvement. (g) K^+–Cl^- interactions: experimental osmotic pressure (red) and osmotic pressure calculated from simulations using the default force field (black). The osmotic pressure obtained from simulations in which the K^+ Lennard-Jones parameters were changed as in the Glu/Asp–K^+ optimization is shown in light blue. This change makes K^+–Cl^- interactions too strong, which is reflected in an osmotic pressure that is too low. To correct this, we modified the K^+–Cl^- Lennard-Jones parameters. Increasing K^+–Cl^- σ weakens K^+–Cl^- interactions, as seen from the increase in osmotic pressure (purple symbols). After optimizing K^+–Cl^- σ, we also adjusted K^+–Cl^- ϵ to match the experimental K^+–Cl^- coordination number at near-saturation concentration (inset). Decreasing K^+–Cl^- ϵ moderately decreases the calculated osmotic pressure (green symbols) while bringing the coordination number into the experimental range. (h) Na^+–Cl^- interactions: experimental osmotic pressure (red) and osmotic pressure calculated from simulations using the default force field (black). The osmotic pressure obtained from simulations in which the Na^+ Lennard-Jones parameters were changed as in the Glu/Asp–Na^+ optimization is shown in light blue. In contrast to K^+–Cl^-, where increasing the K^+ size makes K^+–Cl^- interactions too favorable, increasing the Na^+ size improves agreement with the experimental osmotic pressure. To obtain a Na^+–Cl^- coordination number at near-saturation concentration that agrees with experiment, we further modified Na^+–Cl^- ϵ (green symbols). The final parameter set is highlighted in bold in each panel

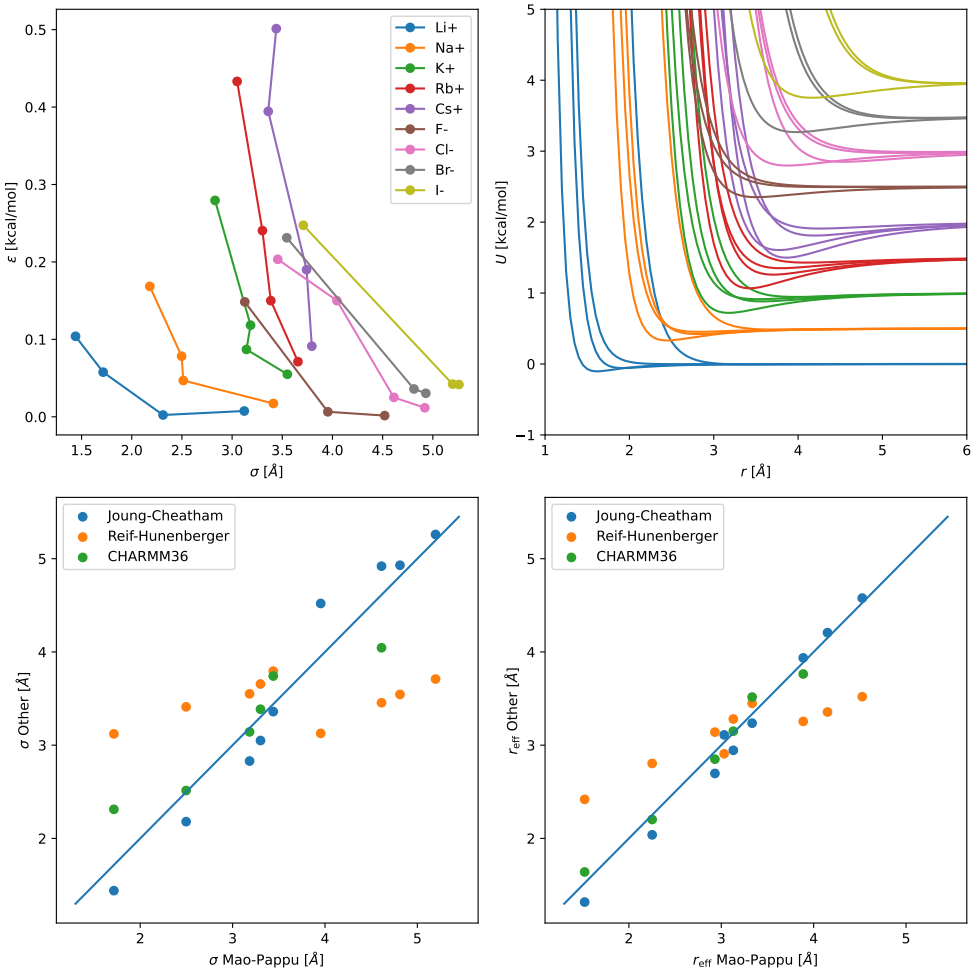

Figure S7: Effective ion radius in recent force fields (a) Anti-correlation between Lennard-Jones σ and ϵ for monovalent ion parameters from Mao and Pappu,[4] Joung and Cheatham,[5] Reif and Hünenberger (M_E parameters)[6] and CHARMM36.[7] (b) Corresponding Lennard-Jones potentials (colors as in (a)). (c) Correlation between Mao-Pappu parameters for σ and those from other force fields (see Legend). (d) Correlation between Mao-Pappu effective radii r_{eff} (as defined in main text) and those from other force fields.

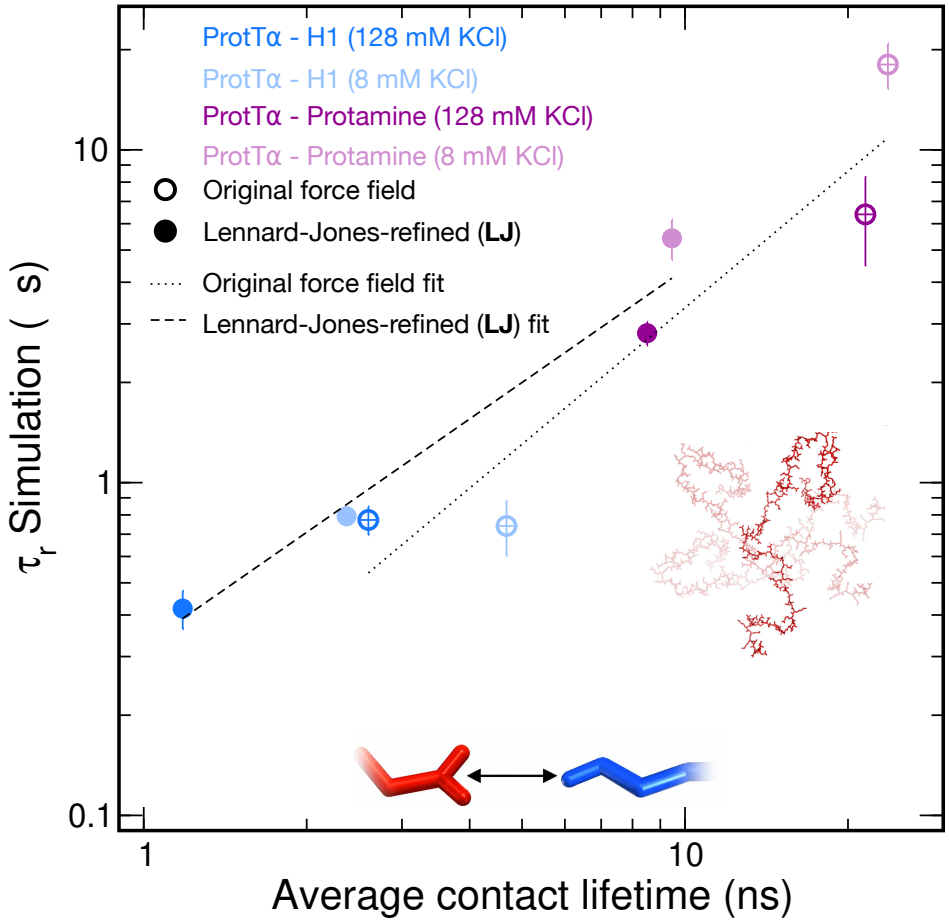

Figure S8: Relation between intermolecular residue–residue contact lifetimes and ProTα chain reconfiguration times in condensates. ProTα reconfiguration times calculated from the simulations are shown as a function of the mean lifetime of intermolecular residue–residue contacts involving ProTα. Contact lifetimes were averaged over all ProTα residues and all 96 ProTα chains in each simulation. Dotted and dashed lines show separate log–log fits to the Amber ff99SBws and Amber ff99SBws-LJ data, respectively. For each force field, the four condensate data points were fitted by ordinary least squares after transforming both variables to $\log_{10}$ scale, that is, $\log_{10} y = a \log_{10} x + b$. Contact lifetimes and chain reconfiguration times are strongly correlated across the four condensates for both force fields. For every condensate, Amber ff99SBws-LJ gives shorter contact lifetimes and shorter reconfiguration times than Amber ff99SBws, with the reconfiguration times in substantially better agreement with experiment (Fig. 5).

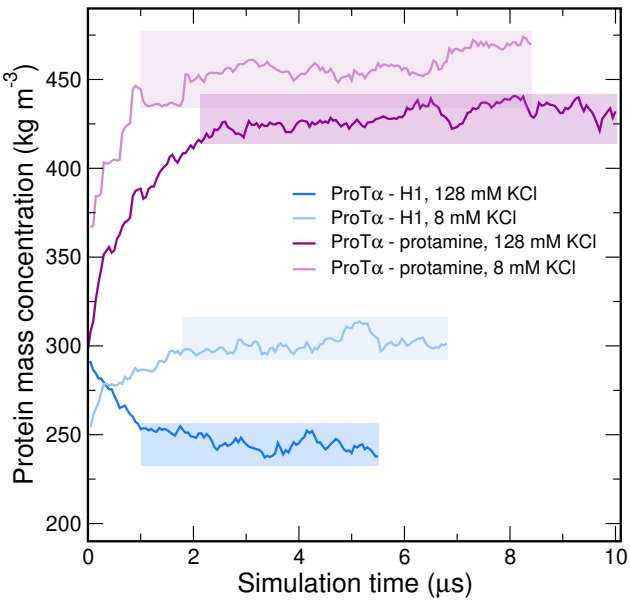

Figure S9: Protein mass concentration as a function of simulation time. Protein mass concentrations in the dense phases were calculated in 50 ns blocks. Initial trajectory segments during which the protein concentration changed substantially were treated as equilibration and excluded from all analyses. Shaded regions indicate the trajectory segments used for the analyses reported in the manuscript. Amber ff99SBws-LJ gives lower mean dense-phase protein concentrations than Amber ff99SBws in all four systems. The concentrations decreased from $(290 \pm 10)\,\mathrm{kg\,m^{-3}}$ to $(245 \pm 5)\,\mathrm{kg\,m^{-3}}$ for ProTα–H1 at 128 mM KCl,[8] from $(339 \pm 5)\,\mathrm{kg\,m^{-3}}$ to $(301 \pm 5)\,\mathrm{kg\,m^{-3}}$ for ProTα–H1 at 8 mM KCl,[9] from $(460 \pm 3)\,\mathrm{kg\,m^{-3}}$ to $(429 \pm 6)\,\mathrm{kg\,m^{-3}}$ for ProTα–protamine at 128 mM KCl,[9] and from $(473 \pm 6)\,\mathrm{kg\,m^{-3}}$ to $(455 \pm 4)\,\mathrm{kg\,m^{-3}}$ for ProTα–protamine at 8 mM KCl.[9] In each comparison, the first value was obtained with Amber ff99SBws and the second with Amber ff99SBws-LJ. These changes correspond to decreases of approximately 16%, 11%, 7%, and 4%, respectively. For the protamine-containing condensates, the dense-phase protein concentration differs by only 4–7% between the two parameter sets, whereas the chain reconfiguration times differ by approximately threefold (Fig. 5 and Table S1), suggesting that dense-phase protein concentration is not the only key factor defining IDP conformational dynamics within condensates.

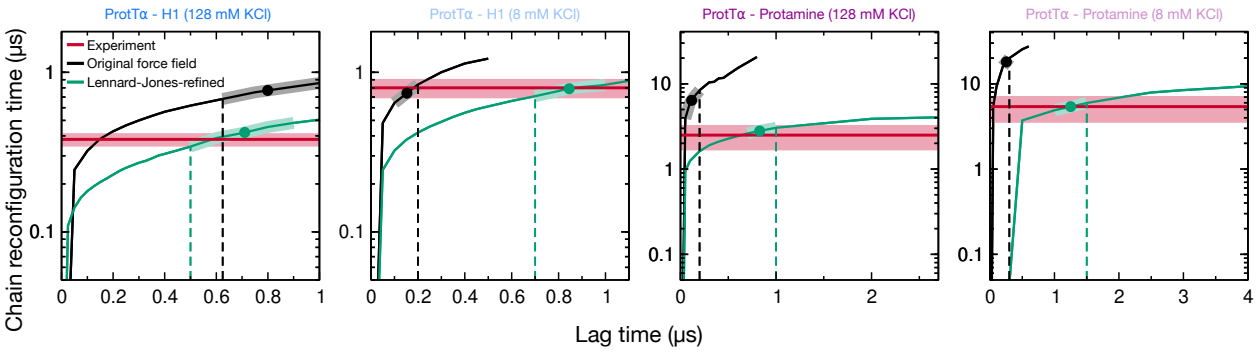

Figure S10: ProTα chain reconfiguration time as a function of diffusion model lag time. For each simulated condensate, the reconfiguration time of ProTα is shown as a function of the lag time used to construct a one-dimensional diffusion model from the distances between residues 58 and 112 of all ProTα chains. Black and green curves show results obtained with Amber ff99SBws and Amber ff99SBws-LJ, respectively. Vertical dashed lines mark the selected lag for each simulation: the smallest candidate lag satisfying the CK criterion or, when no candidate passed, the lag with the lowest CK score. Shaded curve segments indicate the lag-time windows used for averaging. The reported simulated reconfiguration time is the unweighted mean of the reconfiguration times calculated at the candidate lags within each window, and its uncertainty is their sample standard deviation. Filled circles show these mean values. Because an averaged value does not itself have an associated lag, each circle is positioned horizontally by interpolation along the corresponding curve; this position is used only for display. Experimental reconfiguration times and their uncertainties are shown by the red lines and shaded bands, respectively. Further details of the lag-time selection and CK analysis are provided in Methods.

Supporting Tables

Table S1: Mean FRET efficiencies, $\langle E \rangle$, and ProTα chain reconfiguration times, τ_r, are shown for ProTα–H1 and ProTα–protamine condensates at the 8 and 128 mM KCl simulation conditions. Experiments were performed in TEK buffer, which contributes approximately 8 mM to the ionic strength; thus, 0 and 120 mM added KCl in experiment correspond to the 8 and 128 mM simulation conditions. Experimental $\langle E \rangle$ values were measured directly for ProTα–H1 at 8 mM (0.45 ± 0.03),[9] ProTα–H1 at 128 mM (0.45 ± 0.03),[8] and ProTα–protamine at 128 mM (0.54 ± 0.03).[9] For ProTα–protamine at 8 mM, $\langle E \rangle$ was extrapolated using an unweighted quadratic least-squares fit to all six measured salt concentrations,[9] giving $\langle E \rangle = 0.56$. The extrapolation uncertainty (0.014) was combined in quadrature with the experimental uncertainty of 0.03, giving 0.04. For comparison, the closest measured value is $\langle E \rangle = 0.56 \pm 0.03$ at 25 mM added KCl (approximately 33 mM total ionic strength). Simulation uncertainties in $\langle E \rangle$ are standard deviations across the time-averaged transfer efficiencies of 96 ProTα chains. Experimental τ_r values were measured by nsFCS. For ProTα–protamine at 8 mM, the closest experimental τ_r was measured at 25 mM added KCl (approximately 33 mM total ionic strength), because lower-salt measurements were not feasible.[9] Simulations used Amber ff99SBws ("Original") and its Lennard–Jones-refined variant ("LJ-refined"). Simulation uncertainties in τ_r are defined in Methods.

Condensate	KCl (mM)		$\langle E \rangle$	τ_r (μs)
ProTα–H1	128	Experiment	0.45 ± 0.03	0.38 ± 0.04
		Original	0.46 ± 0.18	0.77 ± 0.08
		LJ-refined	0.42 ± 0.14	0.42 ± 0.06
ProTα–H1	8	Experiment	0.45 ± 0.03	0.80 ± 0.12
		Default	0.43 ± 0.27	0.74 ± 0.14
		LJ-refined	0.43 ± 0.16	0.79 ± 0.05
ProTα–protamine	128	Experiment	0.54 ± 0.03	2.5 ± 0.9
		Default	0.50 ± 0.33	6.4 ± 2.0
		LJ-refined	0.50 ± 0.25	2.8 ± 0.3
ProTα–protamine	8	Experiment	0.56 ± 0.04	5.4 ± 2.0[a]
		Default	0.47 ± 0.33	18.1 ± 2.8
		LJ-refined	0.54 ± 0.25	5.4 ± 0.8

[a]Experimental τ_r measured at 25 mM added KCl (approximately 33 mM total ionic strength in TEK buffer) and used for comparison with the ProTα–protamine simulation at 8 mM KCl.

References

(1) Miller, M. S.; Lay, W. K.; Elcock, A. H. Osmotic pressure simulations of amino acids and peptides highlight potential routes to protein force field parameterization. *J. Phys. Chem. B* **2016**, *120*, 8217–8229.

(2) Ivanović, M. T.; Bruetzel, L. K.; Shevchuk, R.; Lipfert, J.; Hub, J. S. Quantifying the influence of the ion cloud on SAXS profiles of charged proteins. *Phys. Chem. Chem. Phys.* **2018**, *20*, 26351–26361.

(3) Lukasheva, N.; Tolmachev, D.; Martinez-Seara, H.; Karttunen, M. Changes in the local conformational states caused by simple Na+ and K+ ions in polyelectrolyte simulations: Comparison of seven force fields with and without NBFIX and ECC corrections. *Polymers* **2022**, *14*, 252.

(4) Mao, A. H.; Pappu, R. V. Crystal lattice properties fully determine short-range interaction parameters for alkali and halide ions. *J. Chem. Phys.* **2012**, *137*.

(5) Joung, I. S.; Cheatham III, T. E. Determination of alkali and halide monovalent ion parameters for use in explicitly solvated biomolecular simulations. *J. Phys. Chem. B* **2008**, *112*, 9020–9041.

(6) Reif, M. M.; Hünenberger, P. H. Computation of methodology-independent single-ion solvation properties from molecular simulations. IV. Optimized Lennard-Jones interaction parameter sets for the alkali and halide ions in water. *J. Chem. Phys.* **2011**, *134*.

(7) Vanommeslaeghe, K.; MacKerell Jr, A. CHARMM additive and polarizable force fields for biophysics and computer-aided drug design. *Biochim. Biophys. Acta, Gen. Subj.* **2015**, *1850*, 861–871.

(8) Galvanetto, N.; Ivanović, M. T.; Chowdhury, A.; Sottini, A.; Nüesch, M. F.; Nettels, D.;

Best, R. B.; Schuler, B. Extreme dynamics in a biomolecular condensate. *Nature* **2023**, *619*, 876–883.

(9) Galvanetto, N.; Ivanović, M. T.; Del Grosso, S. A.; Chowdhury, A.; Sottini, A.; Nettels, D.; Best, R. B.; Schuler, B. Material properties of biomolecular condensates emerge from nanoscale dynamics. *Proc. Natl. Acad. Sci. U.S.A.* **2025**, *122*, e2424135122.